PHYSICAL REVIEW APPLIED **9,** 044025 (2018)

Theory of Excitation Transfer between Two-Dimensional Semiconductor and Molecular Layers

Judith F. Specht,[1,*] Eike Verdenhalven,[1] Björn Bieniek,[2] Patrick Rinke,[2,3] Andreas Knorr,[1] and Marten Richter[1,†]
[1]*Institut für Theoretische Physik, Nichtlineare Optik und Quantenelektronik,*
Technische Universität Berlin, Hardenbergstraße 36, 10623 Berlin, Germany
[2]*Fritz-Haber-Institut der Max-Planck-Gesellschaft, Faradayweg 4-6, 14195 Berlin, Germany*
[3]*Department of Applied Physics, Aalto University, P.O. Box 11100, Aalto FI-00076, Finland*

(Received 12 October 2017; revised manuscript received 12 February 2018; published 18 April 2018)

The geometry-dependent energy transfer rate from an electrically pumped inorganic semiconductor quantum well into an organic molecular layer is studied theoretically. We focus on Förster-type nonradiative excitation transfer between the organic and inorganic layers and include quasimomentum conservation and intermolecular coupling between the molecules in the organic film. (Transition) partial charges calculated from density-functional theory are used to calculate the coupling elements. The partial charges describe the spatial charge distribution and go beyond the common dipole-dipole interaction. We find that the transfer rates are highly sensitive to variations in the geometry of the hybrid inorganic-organic system. For instance, the transfer efficiency is improved by up to 2 orders of magnitude by tuning the spatial arrangement of the molecules on the surface: Parameters of importance are the molecular packing density along the effective molecular dipole axis and the distance between the molecules and the surface. We also observe that the device performance strongly depends on the orientation of the molecular dipole moments relative to the substrate dipole moments determined by the inorganic crystal structure. Moreover, the operating regime is identified where inscattering dominates over unwanted backscattering from the molecular layer into the substrate.

DOI: 10.1103/PhysRevApplied.9.044025

I. INTRODUCTION

A potential advantage of hybrid inorganic-organic systems over their individual constituents is that a synergistic combination can lead to enhanced optoelectronic properties and tunable functionality [1–9]. Typical components include organic materials such as organic dye molecules, and inorganic semiconductor nanostructures such as a quantum well (QW) or a semiconductor surface [10–14]. Inorganic semiconductors have several favorable properties, such as high charge carrier mobilities and efficient carrier injection, that could be beneficially combined with the high radiative emission efficiency of organic molecules due to the strong light-matter coupling. Furthermore, different types of excitation processes can emerge in hybrid nanostructures, e.g., Frenkel-Wannier excitons [15,16] and hybrid charge-transfer interface states (i.e., excitons with the electron and hole located at different constituents of the inorganic-organic heterostructure) [17,18]. In this work, we theoretically study dipole-dipole-interaction-induced excitation transfer pathways (so-called Förster coupling) from an electrically pumped inorganic substrate across a two-dimensional buffer-layer interface towards a layer consisting of organic molecules.

Förster interaction is a nonradiative energy transfer [19] where the excitation energy is transferred from an initially excited donor dipole to an acceptor dipole via a nonretarded dipole-dipole interaction. As a rule of thumb, it requires a spectral overlap of the two dipole resonances in the inorganic substrate and the organic adsorbate. It can couple electronic states in an inorganic semiconductor nanostructure to Frenkel excitons in the organic component and dominates if wave-function overlap between the organic and the inorganic layer is negligible. Such excitation transfer processes have been the object of experimental [2,3,7,20,21] as well as theoretical studies [15,22,23]. However, since a thorough experimental characterization of the underlying microscopic coupling mechanisms is difficult, theoretical studies can extend knowledge towards a detailed understanding of the excitation transfer dynamics in hybrid systems.

In this paper, we derive the Coulomb-induced excitation transfer rate from a ZnO quantum well into a monolayer of organic molecules adsorbed on top of the semiconductor substrate. Our approach represents the case of exciting the optically active organic molecular layer by strong electrical pumping of the semiconductor QW. We focus on the coupling of electrically pumped—i.e., occupied—electron-hole continuum states of the semiconductor to the molecular excitons. The semiconductor continuum covers a broad

---

[*] specht@itp.tu-berlin.de
[†] marten.richter@tu-berlin.de

energy range, which makes the coupling efficiency less sensitive to resonance energy mismatches between the organic and inorganic components. We find that the effect of interlayer coupling is determined by microscopic quasimomentum selection rules that depend on the geometry of the hybrid structure. Therefore, the parameter studies presented in this paper can help to increase the energy transfer efficiency by geometry optimization of the hybrid structure.

We use a density-matrix formalism (similar to Ref. [23]) to study the excitation transfer in the composite inorganic-organic system. For the interactions, we include interlayer Coulomb coupling (Förster type and electrostatic), as well as intermolecular coupling within the organic layer. The intermolecular coupling leads to the formation of bands in the organic system, which is particularly relevant in the case of densely packed molecular films, and thus for small intermolecular distances. Besides the dipole-dipole excitation transfer contributions to the Coulomb Hamiltonian, all electrostatic monopole-monopole coupling terms are also considered, resulting in electrostatic shifts in the resonance energies that strongly depend on the molecular coverage. The microscopic Coulomb coupling elements are calculated using (transition) partial charges [24,25] obtained from density-functional theory (DFT). This approach allows for a more accurate modeling of Coulomb interaction processes for small distances between the interacting constituents compared to a simple point-dipole approximation. We assume a periodic arrangement of the molecules in the organic layer, as in Ref. [23]. In this way, it is possible to consistently treat both the semiconductor and molecular quantities using a quasimomentum representation [23].

This work is organized as follows: First, we illustrate the theoretical treatment of the model system employing a partial-charge approximation of the Coulomb coupling elements (Sec. II). In Sec. III, equations of motion for the excitation transfer are derived for the system density operator, and the scattering rate is deduced. Finally, we present the numerical evaluation using microscopic input parameters obtained from DFT calculations (Sec. IV).

II. MODEL SYSTEM AND HAMILTONIAN

A. Model system and input parameters

In the considered model system, flat ladder-type quarterphenyl (L4P) molecules [26] are arranged in a quasi-two-dimensional film on a ZnO QW; see Fig. 1(a). The microscopic input parameters are taken from DFT calculations. The adsorption geometry is calculated for an organic film of weakly bonded L4P molecules relaxed on top of a $\mathrm{ZnO}(10\bar{1}0)$ surface. This geometry is kept fixed for deriving the partial charges of the organic and inorganic component in separate DFT calculations in vacuum. The DFT calculations employ the hybrid exchange-correlation (xc) functional Heyd-Scuseria-Ernzerhof (HSE06) [27] as implemented in the FHI-aims code [28–30]. We use *tight* numerical settings for all calculations. Relativistic effects are accounted for by the *atomic zeroth-order regular approximation* approach [28]. The substrate is modeled using the slab approach, where a ZnO unit cell with a z extension corresponding to a QW thickness of 4.3 nm is defined and repeated periodically. The periodic images of the slab are separated by a vacuum layer >30 Å in the z direction. Potential electrostatic interactions between periodic images are compensated for by a dipole correction [31]. For the integrations over the Brillouin zone for obtaining the transition partial charges, we use a k-point grid with a density of 4 points per Å^{-1} in the directions corresponding to the surface plane. Van der Waals interactions are taken into account by means of the Tkatchenko-Scheffler (TS) scheme [32]. For the ZnO surface, the TS parametrization of Ref. [33] is used (see Refs. [34,35] for details).

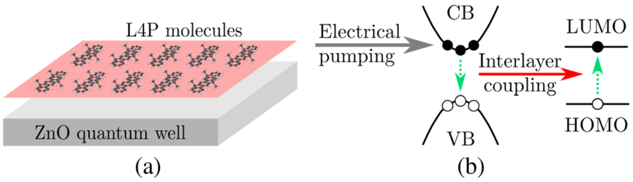

(a) (b)

FIG. 1. (a) Model system consisting of a single layer of L4P molecules adsorbed on a ZnO substrate. (b) Schematic of Förster energy transfer from an electrically pumped semiconductor to a molecule.

B. Hamiltonian

We focus on the energetically lowest allowed electronic transitions between the highest occupied molecular orbital (HOMO, H) and lowest unoccupied molecular orbital (LUMO, L) in the molecules and between the valence and conduction bands in the semiconductor substrate. The Hamilton operator of the hybrid system for calculating the transfer rate consists of three parts: $\hat{H} = \hat{H}_0 + \hat{H}_C^{m\text{-}m} + \hat{H}_C^{m\text{-}s}$.

The Hamiltonian

$$\hat{H}_0 = \hat{H}_0^m + \hat{H}_0^s = \sum_{A,\nu} \varepsilon_A^\nu \hat{a}_{A,\nu}^\dagger \hat{a}_{A,\nu} + \sum_{\lambda,\boldsymbol{k}} \varepsilon_\lambda^{\boldsymbol{k}} \hat{a}_{\lambda,\boldsymbol{k}}^\dagger \hat{a}_{\lambda,\boldsymbol{k}} \quad (1)$$

contains the free-particle energies ε_A^ν and $\varepsilon_\lambda^{\boldsymbol{k}}$ of the carriers in the molecular layer and in the semiconductor bands, respectively. The index A (running over H and L) denotes the molecular orbital of the νth molecule with the electronic wave function $\psi_{A,\nu}$. Since we assume identical molecules, $\varepsilon_A^\nu \equiv \varepsilon_A$ holds. λ includes the valence (v) and conduction (c) band and $\boldsymbol{k} \equiv \boldsymbol{k}_\parallel$ the (two-dimensional) wave vector of a semiconductor electron in the two-dimensional QW plane with wave function $\psi_{\lambda,\boldsymbol{k}}$ in the envelope-function approximation [10]. $\hat{a}_{A,\nu}^{(\dagger)}$ and $\hat{a}_{\lambda,\boldsymbol{k}}^{(\dagger)}$ are the annihilation (creation) operators for an electron in a molecule and in the semiconductor QW, respectively.

We consider two different contributions from the Coulomb interaction. First, $\hat{H}_C^{m\text{-}m}$ describes the intermolecular coupling between molecules in the organic layer:

$$\hat{H}_C^{m\text{-}m} = \frac{1}{2}\sum_{A,B}\sum_{\nu_a\neq\nu_b} V_{A,\nu_a\ B,\nu_b}^{A,\nu_a\ B,\nu_b}\hat{a}_{A,\nu_a}^{\dagger}\hat{a}_{B,\nu_b}^{\dagger}\hat{a}_{B,\nu_b}\hat{a}_{A,\nu_a} + \sum_{\nu_a\neq\nu_b} V_{L,\nu_a\ H,\nu_b}^{H,\nu_a\ L,\nu_b}\hat{a}_{H,\nu_a}^{\dagger}\hat{a}_{L,\nu_b}^{\dagger}\hat{a}_{H,\nu_b}\hat{a}_{L,\nu_a}, \tag{2}$$

with the Coulomb coupling matrix element

$$V_{A',\nu_a\ B',\nu_b}^{A,\nu_a\ B,\nu_b} = \int d^3r\int d^3r'\psi_{A,\nu_a}^{*}(\boldsymbol{r})\psi_{B,\nu_b}^{*}(\boldsymbol{r}') \times e^2G^{m\text{-}m}(\boldsymbol{r},\boldsymbol{r}')\psi_{B',\nu_b}(\boldsymbol{r}')\psi_{A',\nu_a}(\boldsymbol{r}). \tag{3}$$

$G^{m\text{-}m}(\boldsymbol{r},\boldsymbol{r}')$ denotes the Green's functions for the Coulomb interaction between two charges at $\boldsymbol{r}$ and $\boldsymbol{r}'$, as it arises from Poisson's equation for interacting charges and is discussed later in this section. Note that we distinguish two contributions in Eq. (2) [36]: The diagonal monopole-monopole coupling (the first term) represents the electrostatic Coulomb interaction between charge densities and gives rise to an energy renormalization of the electronic states. The off-diagonal Förster coupling (the second term) describes an excitation energy transfer.

Second, the molecule-semiconductor (interlayer) Coulomb Hamiltonian $\hat{H}_C^{m\text{-}s}$ describes the coupling between the molecules and the electrons in the semiconductor substrate; see Fig. 1(b):

$$\hat{H}_C^{m\text{-}s} = \sum_{\lambda,\boldsymbol{k},\boldsymbol{k}'}\sum_{A,\nu} V_{\lambda,\boldsymbol{k}'\ A,\nu}^{\lambda,\boldsymbol{k}\ A,\nu}\hat{a}_{\lambda,\boldsymbol{k}}^{\dagger}\hat{a}_{A,\nu}^{\dagger}\hat{a}_{A,\nu}\hat{a}_{\lambda,\boldsymbol{k}'} + \left(\sum_{\boldsymbol{k},\boldsymbol{k}'}\sum_{\nu} V_{v,\boldsymbol{k}'\ L,\nu}^{\mathrm{c},\boldsymbol{k}\ H,\nu}\hat{a}_{c,\boldsymbol{k}}^{\dagger}\hat{a}_{H,\nu}^{\dagger}\hat{a}_{L,\nu}\hat{a}_{v,\boldsymbol{k}'} + \mathrm{H.c.}\right), \tag{4}$$

$$V_{\lambda',\boldsymbol{k}'\ B,\nu}^{\lambda,\boldsymbol{k}\ A,\nu} = \int d^3r\int d^3r'\psi_{\lambda,\boldsymbol{k}}^{*}(\boldsymbol{r})\psi_{A,\nu}^{*}(\boldsymbol{r}') \times e^2G^{m\text{-}s}(\boldsymbol{r},\boldsymbol{r}')\psi_{B,\nu}(\boldsymbol{r}')\psi_{\lambda',\boldsymbol{k}'}(\boldsymbol{r}). \tag{5}$$

Couplings such as the Coulomb interaction between the semiconductor electrons within the QW substrate are not considered here since our goal is to describe strong, incoherent electrical pumping of the semiconductor with large carrier densities, which suppresses the formation of Wannier-exciton-like bound states within the semiconductor.

The dielectric screening in the composite system is taken into account by introducing effective dielectric constants $\epsilon_{\mathrm{eff}}^{m\text{-}m}=\epsilon_m(\epsilon_s+\epsilon_m)/(\epsilon_s-\epsilon_m)$ for the intermolecular and $\epsilon_{\mathrm{eff}}^{m\text{-}s}=\frac{1}{2}(\epsilon_s+\epsilon_m)$ for the interlayer Coulomb matrix elements. The effective dielectric constants are derived treating two half-spaces with different bulk dielectrics, ϵ_m in the molecular layer and ϵ_s in the semiconductor substrate. Electrostatic charges within one of the half-spaces influence the electrostatic potential in the other half-space, which can be described using the concept of image charges; see Refs. [37,38]. The Green's functions are given by

$$G^{m\text{-}m}(\boldsymbol{r},\boldsymbol{r}') = \frac{1}{4\pi\epsilon_0}\left(\frac{1}{\epsilon_m|\boldsymbol{r}-\boldsymbol{r}'|} - \frac{1}{\epsilon_{\mathrm{eff}}^{m\text{-}m}\sqrt{(x-x')^2+(y-y')^2+(z+z')^2}}\right) \tag{6}$$

for the intermolecular and

$$G^{m\text{-}s}(\boldsymbol{r},\boldsymbol{r}') = \frac{1}{4\pi\epsilon_0\epsilon_{\mathrm{eff}}^{m\text{-}s}}\frac{1}{|\boldsymbol{r}-\boldsymbol{r}'|} \tag{7}$$

for the interlayer Coulomb interaction.

C. Partial-charge approximation

A dipole approximation is a common procedure for deriving Coulomb coupling elements for excitation energy transfer (see, e.g., Refs. [39–43]). However, the approximation is questionable if the size of the interacting wave functions is on the same order as the distance between the two constituents (i.e., in the case of intermolecular coupling). One way to overcome this limitation is the extended dipole approximation [24]. Here, a well-known method from the force-field community and quantum chemistry is adapted, using partial charges that are obtained numerically by fitting the electrostatic potential [44–52].

In Ref. [24], this partial-charge technique was used to describe two strongly coupled pigments in light-harvesting complexes, each given by a many-particle wave function containing N electrons. Here, we have a Hamiltonian in second quantization. We define the single-particle density $\rho_{\nu}^{AB}(\boldsymbol{r})$ of the νth molecule as the product of two molecular wave functions [53]: $\rho_{\nu}^{AB}(\boldsymbol{r}) = \psi_{A,\nu}^{*}(\boldsymbol{r})\psi_{B,\nu}(\boldsymbol{r})$. For $A\neq B$, it represents the HOMO-LUMO transition density. We introduce the potential solving the Poisson equation with mirror charges $\Delta_{\boldsymbol{r}}\phi_{\nu_b}^{BB'}(\boldsymbol{r})=e/\epsilon_0[\rho_{\nu_b}^{BB'}(\boldsymbol{r})/\epsilon_m-\rho_{\nu_b}^{BB'}(x,y,-z)/\epsilon_{\mathrm{eff}}^{m\text{-}m}]$,

$$\phi_{\nu_b}^{BB'}(\boldsymbol{r}) = -\int d^3r'eG^{m\text{-}m}(\boldsymbol{r},\boldsymbol{r}')\rho_{\nu_b}^{BB'}(\boldsymbol{r}'), \tag{8}$$

of molecule ν_b and approximate it by the potential generated by point charges, the atomic partial charges $q_j^{BB'}$ at the atomic positions $\boldsymbol{R}_{j_{\nu_b}}$:

$$\phi_{\nu_b}^{BB'}(\boldsymbol{r}) \approx \sum_j G^{m\text{-}m}(\boldsymbol{r},\boldsymbol{R}_{j_{\nu_b}})q_j^{BB'}, \tag{9}$$

where $\boldsymbol{R}_{j_{\nu_b}} = \boldsymbol{R}_{\nu_b}+\boldsymbol{r}_j$ is the sum of position $\boldsymbol{R}_{\nu_b}$ of molecule ν_b and the position $\boldsymbol{r}_j$ of the jth atom of molecule ν_b relative to $\boldsymbol{R}_{\nu_b}$. Assuming identical, uniformly oriented molecules, these relative positions $\boldsymbol{r}_j$ and charges $q_i^{AB,\nu} \equiv q_i^{AB}$ are equal for all molecules. After introducing the same procedure of generating partial charges for molecule ν_a, the Coulomb coupling is expressed as the electrostatic interaction between atomic partial charges [24]:

$$V^{A,\nu_a\ B,\nu_b}_{A',\nu_a\ B',\nu_b} \approx \sum_{i,j} G^{m\text{-}m}(\boldsymbol{R}_{i_{\nu_a}}, \boldsymbol{R}_{j_{\nu_b}}) q_i^{AA'} q_j^{BB'}. \tag{10}$$

The concept of the partial-charge approximation for intermolecular Coulomb matrix elements can be extended to the interfacial molecule-semiconductor coupling. Therefore, we define the one-particle density of the semiconductor substrate $\rho^{\lambda\lambda'}_{\boldsymbol{k}\boldsymbol{k}'}(\boldsymbol{r}) = \psi^*_{\lambda,\boldsymbol{k}}(\boldsymbol{r})\psi_{\lambda',\boldsymbol{k}'}(\boldsymbol{r})$. We introduce an electrostatic potential for the nth unit cell of the semiconductor substrate and approximate it by the potential of the partial charges $q_i^{\lambda\lambda'}$ at the relative positions $\boldsymbol{r}_i$ within one unit cell:

$$\phi_n^{\lambda\lambda',\boldsymbol{k}\boldsymbol{k}'}(\boldsymbol{r}) = -\frac{1}{A_{\mathrm{u.c.}}}\int_{(\mathrm{u.c.})_n} d^3r' e G^{m\text{-}s}(\boldsymbol{r}, \boldsymbol{R}_i + \boldsymbol{r}') u^*_{\lambda,\boldsymbol{k}}(\boldsymbol{r}') \times u_{\lambda',\boldsymbol{k}'}(\boldsymbol{r}') e^{i(\boldsymbol{k}'-\boldsymbol{k})\cdot\boldsymbol{r}'_\parallel} \xi^*_\lambda(Z_n + z')\xi_{\lambda'}(Z_n + z') \tag{11}$$

$$\approx \sum_i G^{m\text{-}s}(\boldsymbol{r}, \boldsymbol{r}_i) q_i^{\lambda\lambda'}, \tag{12}$$

where $A_{\mathrm{u.c.}}$ denotes the area of the ZnO unit cell, $\boldsymbol{R}_n$ the lattice vector connected to the nth unit cell with the z component Z_n, $u_{\lambda,\boldsymbol{k}}(\boldsymbol{r})$ the lattice-periodic Bloch function, and $\xi^*_\lambda(z)$ the QW envelope function in the z direction. Note that we neglect the momentum dependence of the semiconductor partial charges and take the value at the Γ point: $q_i^{\lambda\lambda',\boldsymbol{k}\boldsymbol{k}'} \approx q_i^{\lambda\lambda',\boldsymbol{0}\boldsymbol{0}} \equiv q_i^{\lambda\lambda'}$. This approximation is valid since we consider only electronic states close to the band edges (see Sec. IV).

To rewrite the matrix element in terms of the approximative partial charges, the integral over $\boldsymbol{r}$ in Eq. (5) is transformed into a sum of integrals over the single unit cells, and the invariance of the Bloch functions under a lattice translation is used:

$$V^{\lambda,\boldsymbol{k}\ A,\nu}_{\lambda',\boldsymbol{k}'\ B,\nu} \approx \frac{1}{N_{\mathrm{u.c.}}}\sum_{n=1}^{N_{\mathrm{u.c.}}} e^{i(\boldsymbol{k}'-\boldsymbol{k})\cdot\boldsymbol{R}_{n\parallel}} \times \sum_{i,j} G^{m\text{-}s}(\boldsymbol{R}_\nu + \boldsymbol{r}_j, \boldsymbol{R}_n + \boldsymbol{r}_i) q_i^{\lambda\lambda'} q_j^{AB}. \tag{13}$$

$N_{\mathrm{u.c.}}$ is the total number of unit cells in the QW.

In this way, the complex field distribution of the molecules and the semiconductor outside the van der Waals radius of the atoms are represented by point charges at the atomic positions. The partial-charge technique can be applied if the electrostatic potentials are known, e.g., from DFT calculations. A detailed description of how the partial charges are calculated in FHI-aims is given in Appendix A. The partial charges obtained by a fitting to the electrostatic potential from a DFT calculation give direct access to the effective transition dipole moment by summing over the charges at the atomic positions

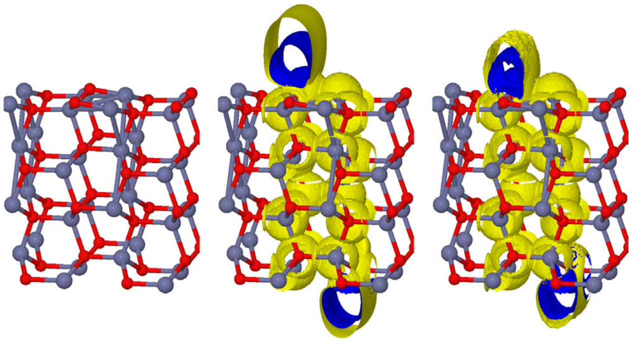
(a) (b) (c)

FIG. 2. (a) Atomic structure of the ZnO $(10\bar{1}0)$ surface. (b) Electrostatic potential obtained from a DFT calculation employing the hybrid xc functional HSE06 [27]. (c) Electrostatic potential of the ZnO $(10\bar{1}0)$ surface generated by the approximate partial charges. The calculated electrostatic potential of (b) is well represented by the reconstruction with partial charges. The unit cell is periodically extended perpendicular to the surface.

$$\boldsymbol{d}_{cv} = \sum_i q_i^{cv}\boldsymbol{r}_i. \tag{14}$$

Analogously, the effective dipole moment of the L4P molecule is given by:

$$\boldsymbol{d}_{LH} = \sum_j q_j^{LH}\boldsymbol{r}_j. \tag{15}$$

The *full* electrostatic potential is required for calculating the partial charges $q_i^{\lambda\lambda}$ and q_j^{AA} that enter the monopole-monopole coupling elements. It is typically calculated by solving the Poisson equation for the full density. In FHI-aims, a very efficient algorithm is used that employs the multipole moments of the density [54,55]. To approximate the Förster-type coupling elements, we need to calculate the *transition* partial charges $q_i^{\lambda\lambda'}$ $(\lambda \neq \lambda')$ and q_j^{AB} $(A \neq B)$ for the involved electronic states (orbitals) or, rather, products of states. They can be calculated analogous to the charges calculated for the full potential once the transition potential is calculated. Instead of using the full charge density as input for this algorithm, we implement the option to calculate a transition density. The charges are fitted to the electrostatic potential calculated on different grids based on these transition densities. The potential obtained from a DFT calculation employing the hybrid xc functional HSE06 [27] and the potential reconstructed from the partial charges are shown in Fig. 2.

D. Transformation of molecular orbitals into a Bloch basis

Following Ref. [23], we assume a lattice-periodic arrangement of the organic molecules. Moreover, we assume that the substrate unit cells match the molecule unit cell such that the molecular lattice vectors are integer multiples of the substrate lattice vector, as illustrated in Fig. 3. This assumption leads to an idealized model used for the microscopic description. An extension to a disordered molecular layer is planned for future work [56]. We transform the molecular operators into a Bloch basis using $\hat{a}_{A,\nu} = 1/\sqrt{N_m}\sum_{\boldsymbol{l}} e^{-i\boldsymbol{l}\cdot\boldsymbol{R}_{\nu\parallel}}\hat{a}_{A,\boldsymbol{l}}$ (see Refs. [23,57]), where we introduce the two-dimensional wave vectors $\boldsymbol{l}$ for the molecular states. The wave vectors $\boldsymbol{l}$ are restricted to the first Brillouin zone of the molecules; see Fig. 3. N_m is the total number of molecules. For a sufficiently extended molecular layer, we approximate [23]

$$\sum_{\nu}\frac{1}{N_m}e^{i\boldsymbol{Q}\cdot\boldsymbol{R}_{\nu\parallel}} \approx \sum_{m_1,m_2\in\mathbb{Z}}\delta_{\boldsymbol{Q},m_1\tilde{\boldsymbol{b}}_1+m_2\tilde{\boldsymbol{b}}_2} \equiv \sum_{\boldsymbol{G}_m}\delta_{\boldsymbol{Q},\boldsymbol{G}_m}, \tag{16}$$

with $\boldsymbol{G}_m = m_1\tilde{\boldsymbol{b}}_1 + m_2\tilde{\boldsymbol{b}}_2$ being a lattice vector in molecular reciprocal space (see Fig. 3). The molecular free-electron part in the new basis reads

$$\hat{H}_0^m = \sum_A \varepsilon_A \sum_{\boldsymbol{l}} \hat{a}^\dagger_{A,\boldsymbol{l}}\hat{a}_{A,\boldsymbol{l}}. \tag{17}$$

The intermolecular Coulomb Hamiltonian in the momentum basis has the form

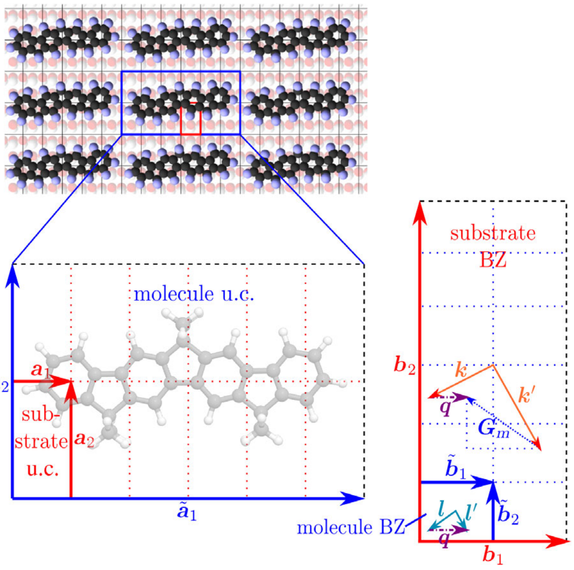

FIG. 3. Unit cells (u.c.'s, left panel) and Brillouin zones (BZs, right panel) of the hybrid system with the maximum coverage of one molecule per 12 substrate unit cells (6 × 2) (see Refs. [23,38]). The momentum vector diagrams depicted in the substrate and molecule BZs illustrate the microscopic momentum selection rules of the interlayer coupling.

$$\begin{aligned}\hat{H}_C^{m\text{-}m} = {}& \frac{1}{2}\frac{1}{N_m}\sum_{A,B}\sum_{\boldsymbol{l}_1,\ldots,\boldsymbol{l}_4}\sum_{\boldsymbol{G}_m}\delta_{\boldsymbol{l}_1-\boldsymbol{l}_4,\boldsymbol{l}_3-\boldsymbol{l}_2+\boldsymbol{G}_m}\mathcal{V}^{A\,B}_{A\,B}(\boldsymbol{l}_2-\boldsymbol{l}_3)\hat{a}^\dagger_{A,\boldsymbol{l}_1}\hat{a}^\dagger_{B,\boldsymbol{l}_2}\hat{a}_{B,\boldsymbol{l}_3}\hat{a}_{A,\boldsymbol{l}_4}\\ &+\frac{1}{N_m}\sum_{\boldsymbol{l}_1,\ldots,\boldsymbol{l}_4}\sum_{\boldsymbol{G}_m}\delta_{\boldsymbol{l}_1-\boldsymbol{l}_4,\boldsymbol{l}_3-\boldsymbol{l}_2+\boldsymbol{G}_m}\mathcal{V}^{H\,L}_{L\,H}(\boldsymbol{l}_2-\boldsymbol{l}_3)\hat{a}^\dagger_{H,\boldsymbol{l}_1}\hat{a}^\dagger_{L,\boldsymbol{l}_2}\hat{a}_{H,\boldsymbol{l}_3}\hat{a}_{L,\boldsymbol{l}_4},\end{aligned} \tag{18}$$

with the coupling element using partial charges,

$$\mathcal{V}^{A\,B}_{A'\,B'}(\boldsymbol{q}) = \sum_{\boldsymbol{\Delta}_{m\text{-}m}\neq\boldsymbol{0}} e^{i\boldsymbol{q}\cdot\boldsymbol{\Delta}_{m\text{-}m\parallel}}\sum_{i,j}q_i^{AA'}q_j^{BB'}G^{m\text{-}m}(\boldsymbol{r}_i,\boldsymbol{r}_j+\boldsymbol{\Delta}_{m\text{-}m}). \tag{19}$$

Here, the sum over $\boldsymbol{\Delta}_{m\text{-}m}\equiv\boldsymbol{R}_{\nu_b}-\boldsymbol{R}_{\nu_a}$ runs over all difference vectors between the positions of two molecular unit cells (with one cell at a fixed position). The Kronecker δ in Eq. (18) ensures momentum conservation, except for a reciprocal lattice vector. The interlayer Coulomb Hamiltonian is also transformed into momentum representation:

$$\begin{aligned}\hat{H}_C^{m\text{-}s} = {}& \frac{1}{N_{\text{u.c.}}}\sum_{\lambda,\boldsymbol{k},\boldsymbol{k}'}\sum_{A,\boldsymbol{l},\boldsymbol{l}'}\sum_{\boldsymbol{G}_m}\delta_{\boldsymbol{l}-\boldsymbol{l}',\boldsymbol{k}-\boldsymbol{k}'+\boldsymbol{G}_m}\mathcal{V}^{\lambda\,A}_{\lambda\,A}(\boldsymbol{k}'-\boldsymbol{k})\hat{a}^\dagger_{\lambda,\boldsymbol{k}}\hat{a}^\dagger_{A,\boldsymbol{l}}\hat{a}_{A,\boldsymbol{l}'}\hat{a}_{\lambda,\boldsymbol{k}'}\\ &+\frac{1}{N_{\text{u.c.}}}\left(\sum_{\boldsymbol{k},\boldsymbol{k}'}\sum_{\boldsymbol{l},\boldsymbol{l}'}\sum_{\boldsymbol{G}_m}\delta_{\boldsymbol{l}-\boldsymbol{l}',\boldsymbol{k}-\boldsymbol{k}'+\boldsymbol{G}_m}\mathcal{V}^{c\,H}_{v\,L}(\boldsymbol{k}'-\boldsymbol{k})\hat{a}^\dagger_{c,\boldsymbol{k}}\hat{a}^\dagger_{H,\boldsymbol{l}}\hat{a}_{L,\boldsymbol{l}'}\hat{a}_{v,\boldsymbol{k}'}+\text{H.c.}\right),\end{aligned} \tag{20}$$

with the redefined matrix elements

$$\mathcal{V}^{\lambda\,A}_{\lambda'\,A'}(\boldsymbol{q}) = \sum_{\boldsymbol{\Delta}_{m\text{-}s}} e^{i\boldsymbol{q}\cdot\boldsymbol{\Delta}_{m\text{-}s\parallel}}\sum_{i,j}q_i^{\lambda\lambda'}q_j^{AA'}G^{m\text{-}s}(\boldsymbol{r}_j,\boldsymbol{r}_i+\boldsymbol{\Delta}_{m\text{-}s}). \tag{21}$$

The sum over $\boldsymbol{\Delta}_{m\text{-}s}\equiv\boldsymbol{R}_i-\boldsymbol{R}_\nu$ runs over the positions $\boldsymbol{R}_i$ of all substrate unit cells relative to a fixed molecular position $\boldsymbol{R}_\nu$. The Kronecker δ in Eq. (20) ensures quasimomentum conservation during Förster transfer and imposes microscopic momentum selection rules on the system. The change in momentum in the molecule has to match the momentum change in the semiconductor substrate except for a reciprocal lattice vector $\boldsymbol{G}_m$ of the molecules; see Fig. 3 (right panel).

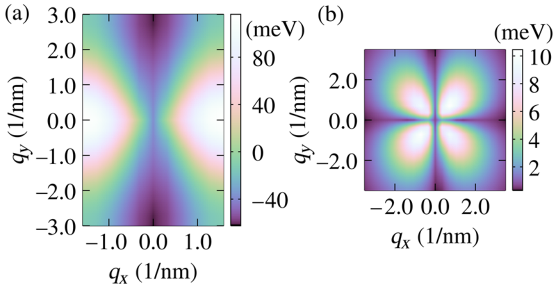

FIG. 4. (a) Contour plot showing the magnitude of the intermolecular Förster coupling element $\mathcal{V}^{H\ L}_{L\ H}(\boldsymbol{q})$ in meV over all $\boldsymbol{q}$ values belonging to the first-molecule Brillouin zone for the maximum coverage of one molecule per 12 substrate unit cells (6×2). (b) Contour plot for the coupling strength $|\mathcal{V}^{c\ H}_{v\ L}(\boldsymbol{q})|$ of the interlayer Förster interaction in meV.

In Fig. 4(a), the intermolecular Förster coupling element $\mathcal{V}^{H\ L}_{L\ H}(\boldsymbol{q})$ is plotted. It exhibits a dumbbell-like shape along the x direction since the effective dipole moments [given in Eq. (15)] of all uniformly oriented molecules in the organic film point in the x direction, such that the maxima of the coupling strength also lie along the x axis [23]. Figure 4(b) shows the interlayer Förster coupling strength $|\mathcal{V}^{c\ H}_{v\ L}(\boldsymbol{q})|$. The shape of the transfer element shows four lobes oriented roughly along the diagonals since the effective dipole moments obtained from the transition partial charges [see Eqs. (14) and (15)] are oriented almost perpendicular to each other along the coordinate axes: $\boldsymbol{d}_{LH} \| \boldsymbol{e}_x$, $\boldsymbol{d}_{cv} \| \boldsymbol{e}_y$.

E. Molecular exciton basis

The state $|\phi^m_0\rangle$ denotes the ground state of the organic layer where the HOMOs of all molecules are fully occupied. A basis describing exciton states is defined using the ground state and the annihilation (creation) operators $\hat{a}^{(\dagger)}_{A,\boldsymbol{l}}$ for electrons in the molecule:

$$|\boldsymbol{l}_1, \boldsymbol{l}_2\rangle \equiv \hat{a}^\dagger_{L,\boldsymbol{l}_1} \hat{a}_{H,\boldsymbol{l}_2} |\phi^m_0\rangle. \tag{22}$$

Owing to the intermolecular Coulomb interaction, the coupled excitonic states of the molecular layer are delocalized superpositions of the two-particle states:

$$|X^m_\alpha\rangle = \sum_{\boldsymbol{l}_1,\boldsymbol{l}_2} c^\alpha_{\boldsymbol{l}_1,\boldsymbol{l}_2} |\boldsymbol{l}_1, \boldsymbol{l}_2\rangle = \sum_{\boldsymbol{l},\boldsymbol{q}} c^\alpha_{\boldsymbol{l}+\boldsymbol{q},\boldsymbol{l}} |\boldsymbol{l}+\boldsymbol{q}, \boldsymbol{l}\rangle. \tag{23}$$

Here, the wave vectors of the exciton basis are given using $\boldsymbol{l} \equiv \boldsymbol{l}_2$ and momentum transfer $\boldsymbol{q} \equiv \boldsymbol{l}_1 - \boldsymbol{l}_2$.

The eigenvalue problem for the molecular Frenkel exciton states $|X^m_\alpha\rangle$ is given by $(\hat{H}^m_0 + \hat{H}^{m\text{-}m}_C)|X^m_\alpha\rangle = (E^m_0 + E^m_\alpha)|X^m_\alpha\rangle$, where we introduce the molecular eigenenergy $E^m_0 + E^m_\alpha$ that solves the Schrödinger equation of the molecular layer. $E^m_0 = \langle\phi^m_0|\hat{H}^m_0 + \hat{H}^{m\text{-}m}_C|\phi^m_0\rangle$ denotes the constant ground-state energy.

A representation of the eigenproblem in the two-particle basis has the form

$$\langle \boldsymbol{l}+\boldsymbol{q}, \boldsymbol{l}|\hat{H}^m_0 + \hat{H}^{m\text{-}m}_C|X^m_\alpha\rangle = (E^m_0 + E^m_\alpha) c^\alpha_{\boldsymbol{l}+\boldsymbol{q},\boldsymbol{l}}, \tag{24}$$

where the left-hand side of the equation depends on the coefficients $c^\alpha_{\boldsymbol{l}+\boldsymbol{q},\boldsymbol{l}}$, according to Eq. (23). Using the Hamiltonian in momentum representation (as derived in Sec. II D), the left-hand side of this equation is evaluated numerically using the discrete wave vectors $\boldsymbol{l}_i$ and $\boldsymbol{q}_j$ (with each having N^m_d values). The calculation is shown in Appendix B. The full molecular eigenproblem is block diagonal with respect to $\boldsymbol{q}_j$, leading to an analytical solution for the eigenenergies $E^m_{\alpha=\boldsymbol{q}_j,n}$ and the eigenvector components $c^{\alpha=\boldsymbol{q}_j,n}_{\boldsymbol{l}_i+\boldsymbol{q}_j,\boldsymbol{l}_i}$. Two solutions emerge. The $N^m_d - 1$ excitonic basis states corresponding to the degenerate eigenvalue E^m_- are pairwise antisymmetric linear combinations of the two-particle basis functions with the equal momentum transfer $\boldsymbol{q}_j$:

$$|X^m_{\boldsymbol{q}_j,n}\rangle = \sqrt{\frac{N_m}{N^m_d}} \frac{1}{\sqrt{2}} (|\boldsymbol{l}_1 + \boldsymbol{q}_j, \boldsymbol{l}_1\rangle - |\boldsymbol{l}_{n+1} + \boldsymbol{q}_j, \boldsymbol{l}_{n+1}\rangle) \tag{25}$$

for $n \in \{1, \ldots, N^m_d - 1\}$. The nondegenerate eigenvalue $E^m_{\boldsymbol{q}_j+}$ belongs to a fully symmetric eigenvector:

$$|X^m_{\boldsymbol{q}_j+}\rangle = \frac{\sqrt{N_m}}{N^m_d} \sum_{i=1}^{N^m_d} |\boldsymbol{l}_i + \boldsymbol{q}_j, \boldsymbol{l}_i\rangle. \tag{26}$$

It appears that, in contrast to $E^m_{\boldsymbol{q}_j+}$, the degenerate eigenenergy E^m_- is dispersionless, i.e., it does not depend on $\boldsymbol{q}_j$. Later, we show that the corresponding antisymmetric eigenvectors form dark states, such that only the symmetric eigenstates contribute to the charge transfer across the hybrid interface.

Here, only a single-excitation basis for molecular excitons is considered, which is a reasonable assumption since the molecular lifetimes in such hybrid systems (tens to hundreds of picoseconds [6]) are smaller or of the same order as the mean excitation transfer times from the electrically pumped substrate into the organic layer, as detailed in Sec. IV. The validity of this assumption is questionable only in the case of very strong interlayer coupling and the resulting comparably long exciton lifetimes in the molecular layer.

III. EQUATIONS OF MOTION OF THE HYBRID SYSTEM

Now we focus on the transfer of semiconductor excitations to the molecules. The equations of motion in the excitonic basis are derived using the von Neumann equation:

$$i\hbar\frac{\partial}{\partial t}\mathrm{tr}_s[\langle a|\hat{O}_s\hat{\rho}|b\rangle] = \mathrm{tr}_s[\langle a|\hat{O}_s[\hat{H},\hat{\rho}]_-|b\rangle] \tag{27}$$

for the density operator $\hat{\rho} \equiv \hat{\rho}_m \otimes \hat{\rho}_s$. a and b are states of the molecular system and $\hat{O}_s$ is an operator of the semiconductor system or the identity. In the following, we are interested in the population of the molecular system $\rho^m_{\boldsymbol{q}_j,n} \equiv \mathrm{tr}_s[\langle X^m_{\boldsymbol{q}_j,n}|\hat{\rho}|X^m_{\boldsymbol{q}_j,n}\rangle]$, assuming approximative spatial homogeneity in the molecular layer (an identical $\boldsymbol{q}_j$ index). We introduce the assisted molecule-semiconductor coherence $\sigma^{\boldsymbol{k},\boldsymbol{k}'}_{\boldsymbol{q}_j,n} \equiv \mathrm{tr}_s[\hat{a}^\dagger_{c,\boldsymbol{k}}\hat{a}_{v,\boldsymbol{k}'}\langle X^m_{\boldsymbol{q}_j,n}|\hat{\rho}|\phi^m_0\rangle]$. We do not express the full system Hamiltonian $\hat{H}$ in the new basis since it is sufficient to evaluate how the Hamiltonian acts on the new basis states. The equation of motion for the exciton density is given by

$$\frac{\partial}{\partial t}\rho^m_{\boldsymbol{q}_j,n} = -\frac{2}{\hbar}\frac{1}{N_{\mathrm{u.c.}}}\tilde{c}_{\boldsymbol{q}_j,n}\sum_{\boldsymbol{k},\boldsymbol{k}'}\sum_{\boldsymbol{G}_m}\delta_{\boldsymbol{q}_j,\boldsymbol{k}'-\boldsymbol{k}+\boldsymbol{G}_m} \times \mathrm{Im}\left[\mathcal{V}^{c\;H}_{v\;L}(\boldsymbol{k}'-\boldsymbol{k})\sigma^{\boldsymbol{k},\boldsymbol{k}'}_{\boldsymbol{q}_j,n}\right], \tag{28}$$

where we define $\tilde{c}_{\boldsymbol{q}_j,n} \equiv (N_m/N^m_d)\sum_i c^{\boldsymbol{q}_j,n}_{\boldsymbol{l}_i+\boldsymbol{q}_j,\boldsymbol{l}_i}$. The Kronecker δ ensures momentum conservation during interlayer Förster transfer; see Fig. 3. Obviously, the molecule-semiconductor coherence between the layers is the source term of the molecular occupation. $\tilde{c}_{\boldsymbol{q}_j,n} = \frac{1}{\sqrt{2}} - \frac{1}{\sqrt{2}}$ vanishes for the antisymmetric solution of the molecular eigenproblem [see Eq. (B10) in Appendix B], such that only the symmetric (bright) states contribute:

$$\frac{\partial}{\partial t}\rho^m_{\boldsymbol{q}_j+} = -\frac{2}{\hbar}\frac{\sqrt{N^m_d}}{N_{\mathrm{u.c.}}}\sum_{\boldsymbol{k},\boldsymbol{k}'}\sum_{\boldsymbol{G}_m}\delta_{\boldsymbol{q}_j,\boldsymbol{k}'-\boldsymbol{k}+\boldsymbol{G}_m} \times \mathrm{Im}\left[\mathcal{V}^{c\;H}_{v\;L}(\boldsymbol{k}'-\boldsymbol{k})\sigma^{\boldsymbol{k},\boldsymbol{k}'}_{\boldsymbol{q}_j+}\right], \tag{29}$$

$$\begin{aligned}\frac{\partial}{\partial t}\sigma^{\boldsymbol{k},\boldsymbol{k}'}_{\boldsymbol{q}_j+} &= \frac{i}{\hbar}(\varepsilon^{\boldsymbol{k}}_c - \varepsilon^{\boldsymbol{k}'}_v - E^m_{\boldsymbol{q}_j+} + \mathcal{V}^{m\text{-}s}_{\mathrm{mono}})\sigma^{\boldsymbol{k},\boldsymbol{k}'}_{\boldsymbol{q}_j+} \\ &\quad + \frac{i}{\hbar}\frac{\sqrt{N^m_d}}{N_{\mathrm{u.c.}}}\sum_{\boldsymbol{G}_m}\delta_{\boldsymbol{q}_j,\boldsymbol{k}'-\boldsymbol{k}+\boldsymbol{G}_m}\mathcal{V}^{c\;H*}_{v\;L}(\boldsymbol{k}'-\boldsymbol{k}) \\ &\quad \times [(1-f_{h,\boldsymbol{k}'})(1-f_{e,\boldsymbol{k}})\rho^m_{\boldsymbol{q}_j+} - f_{h,\boldsymbol{k}'}f_{e,\boldsymbol{k}}\rho^m_0],\end{aligned} \tag{30}$$

with $\rho^m_0 \equiv \mathrm{tr}_s[\langle\phi^m_0|\hat{\rho}|\phi^m_0\rangle]$. The constant shift

$$\begin{aligned}\mathcal{V}^{m\text{-}s}_{\mathrm{mono}} \equiv{}& \frac{N_m}{N_{\mathrm{u.c.}}}[\mathcal{V}^{c\;H}_{c\;H}(\boldsymbol{0}) - \mathcal{V}^{v\;H}_{v\;H}(\boldsymbol{0})] \\ &+ \left(1 - \frac{1}{2}n^{\mathrm{2D}}_h A_{\mathrm{u.c.}}\right)[\mathcal{V}^{v\;H}_{v\;H}(\boldsymbol{0}) - \mathcal{V}^{v\;L}_{v\;L}(\boldsymbol{0})] \\ &+ \frac{1}{2}n^{\mathrm{2D}}_e A_{\mathrm{u.c.}}[\mathcal{V}^{c\;H}_{c\;H}(\boldsymbol{0}) - \mathcal{V}^{c\;L}_{c\;L}(\boldsymbol{0})]\end{aligned} \tag{31}$$

represents the monopole-monopole interaction, where $n^{\mathrm{2D}}_{e\,\mathrm{or}\,h} = N_{e\,\mathrm{or}\,h}/A_{\mathrm{QW}}$ is the two-dimensional carrier density for electrons (e) and holes (h). It describes the self-energy due to the electrostatic coupling of the electronic states in the molecular layer and the semiconductor substrate. For the derivation of the above equations of motion, spatial homogeneity for the fixed semiconductor populations is assumed using $\langle\hat{a}^\dagger_{\lambda,\boldsymbol{k}}\hat{a}_{\lambda,\boldsymbol{k}'}\rangle = \delta_{\boldsymbol{k},\boldsymbol{k}'}\langle\hat{a}^\dagger_{\lambda,\boldsymbol{k}}\hat{a}_{\lambda,\boldsymbol{k}}\rangle$. As a consequence, inhomogeneous monopole-monopole contributions are neglected. A Hartree-Fock factorization is applied to the semiconductor part, and we set $\delta_{\boldsymbol{k}-\boldsymbol{k}',\boldsymbol{G}_m} = \delta_{\boldsymbol{k},\boldsymbol{k}'}\delta_{\boldsymbol{G}_m,\boldsymbol{0}}$ since only those $\boldsymbol{k}$ states close to the Γ point are relevant. The coherences $\langle\hat{a}^\dagger_{v,\boldsymbol{k}}\hat{a}_{c,\boldsymbol{k}'}\rangle$ are assumed to decay rapidly, such that $\langle\hat{a}^\dagger_{v,\boldsymbol{k}_1}\hat{a}_{c,\boldsymbol{k}_2}\rangle\langle\hat{a}^\dagger_{c,\boldsymbol{k}_3}\hat{a}_{v,\boldsymbol{k}_4}\rangle \approx 0$. Moreover, the system is assumed to be in the thermodynamic quasiequilibrium within the valence and conduction bands, such that the subband carrier populations are described by Fermi distribution functions, $f_{i,\boldsymbol{k}} = \{\exp[(\varepsilon^{\boldsymbol{k}}_i - \mu_i)/(k_B T_i)] + 1\}^{-1}$, with $i = e, h$ for electrons and holes [10,58] (see Fig. 5). μ_i denotes the carrier quasiequilibrium chemical potential in the respective bands, and T_i is the nonequilibrium temperature, which can be different for electrons and holes. We focus on situations where only those states close to the Γ point ($\boldsymbol{k} = \boldsymbol{0}$) are populated. Therefore, a description of the band structure around the Γ point using the effective-mass approximation is possible with effective masses $m^*_v < 0$ and $m^*_c > 0$ and $\varepsilon^{\boldsymbol{k}}_h = -(\hbar^2k^2)/(2m^*_v) = -\varepsilon^{\boldsymbol{k}}_v$, $\varepsilon^{\boldsymbol{k}}_e = (\hbar^2k^2)/(2m^*_c) = \varepsilon^{\boldsymbol{k}}_c - \varepsilon^s_{\mathrm{gap}}$. The effective masses $m^*_v = -8.3035m_0$ of the valence and $m^*_c = 1.4463m_0$ of the conduction-band electrons are obtained from a fit to the DFT band structure of ZnO surface bands [23]. The chemical potential for each band of a two-band system is calculated using [10,59]

$$\mu_i = k_B T_i \ln\left[\exp\left(\frac{\pi\hbar^2 n^{\mathrm{2D}}_i}{m_i k_B T_i}\right) - 1\right]. \tag{32}$$

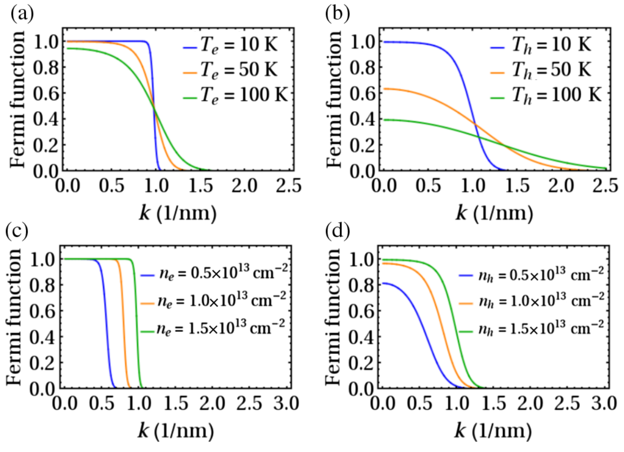

FIG. 5. Fermi functions of (a),(c) electrons and (b),(d) holes for the parameter set given in Table I and (a),(b) varying temperatures and (c),(d) charge carrier concentrations.

The electron-hole states in the semiconductor substrate form a continuum, thus allowing us to solve Eq. (30) for the assisted molecular exciton-substrate polarization $\sigma^{\boldsymbol{k},\boldsymbol{k}'}_{\boldsymbol{q}_j+}$ in the Markov approximation:

$$\sigma^{\boldsymbol{k},\boldsymbol{k}'}_{\boldsymbol{q}_j+} = -i\pi \frac{\sqrt{N^m_d}}{N_{\text{u.c.}}} \sum_{\boldsymbol{G}_m} \delta_{\boldsymbol{q}_j,\boldsymbol{k}'-\boldsymbol{k}+\boldsymbol{G}_m} \mathcal{V}^{c\ H*}_{v\ L}(\boldsymbol{k}'-\boldsymbol{k}) \times (f_{h,\boldsymbol{k}'} f_{e,\boldsymbol{k}} \rho^m_0 - (1-f_{h,\boldsymbol{k}'})(1-f_{e,\boldsymbol{k}})\rho^m_{\boldsymbol{q}_j+}) \times \delta(\varepsilon^{\boldsymbol{k}}_e + \varepsilon^{\boldsymbol{k}'}_h - \Delta_{\boldsymbol{q}_j}), \tag{33}$$

where we introduce $\Delta_{\boldsymbol{q}_j} \equiv E^m_{\boldsymbol{q}_j+} - \varepsilon^s_{\text{gap}} - \mathcal{V}^{m\text{-}s}_{\text{mono}}$. This solution is inserted into the equation of motion for the homogeneous molecule density $\rho^m_{\boldsymbol{q}_j+}$ [Eq. (29)]:

$$\frac{\partial}{\partial t}\rho^m_{\boldsymbol{q}_j+} = \frac{2\pi}{\hbar} \frac{N^m_d}{N^2_{\text{u.c.}}} \sum_{\boldsymbol{k},\boldsymbol{k}'} \sum_{\boldsymbol{G}_m} \delta_{\boldsymbol{q}_j,\boldsymbol{k}'-\boldsymbol{k}+\boldsymbol{G}_m} |\mathcal{V}^{c\ H}_{v\ L}(\boldsymbol{k}'-\boldsymbol{k})|^2 \times (f_{h,\boldsymbol{k}'} f_{e,\boldsymbol{k}} \rho^m_0 - (1-f_{h,\boldsymbol{k}'})(1-f_{e,\boldsymbol{k}})\rho^m_{\boldsymbol{q}_j+}) \times \delta(\varepsilon^{\boldsymbol{k}}_e + \varepsilon^{\boldsymbol{k}'}_h - \Delta_{\boldsymbol{q}_j}). \tag{34}$$

This equation of motion for the transfer from the semiconductor electron-hole continuum to the molecular system allows us to derive microscopic rate equations for (Coulomb) scattering processes in the heterostructure similar to Refs. [60,61].

IV. DISCUSSION OF THE INTERLAYER TRANSFER RATE

From the equation of motion for the population $\rho^m_{\boldsymbol{q}_j+} = \text{tr}_s[\langle X^m_{\boldsymbol{q}_j+}|\hat{\rho}|X^m_{\boldsymbol{q}_j+}\rangle]$ given in Eq. (34), the inscattering rate

$$\Gamma^{\text{in}}_{\boldsymbol{q}_j+} = \frac{2\pi}{\hbar} \frac{N^m_d}{N^2_{\text{u.c.}}} \sum_{\boldsymbol{k},\boldsymbol{k}'} \sum_{\boldsymbol{G}_m} \delta_{\boldsymbol{q}_j,\boldsymbol{k}'-\boldsymbol{k}+\boldsymbol{G}_m} |\mathcal{V}^{c\ H}_{v\ L}(\boldsymbol{k}'-\boldsymbol{k})|^2 \times f_{h,\boldsymbol{k}'} f_{e,\boldsymbol{k}} \delta(\varepsilon^{\boldsymbol{k}}_e + \varepsilon^{\boldsymbol{k}'}_h - \Delta_{\boldsymbol{q}_j}) \tag{35}$$

is identified as the transfer rate from the semiconductor substrate into the exciton state $X^{m+}_{\boldsymbol{q}_j}$ of the molecular layer. It is determined by the interlayer Förster coupling strength, the Fermi functions $f_{h,\boldsymbol{k}'} f_{e,\boldsymbol{k}}$ representing the quasiequilibrium carrier distributions in the QW, and the momentum and energy conservation. In the same way, the backscattering into the semiconductor layer is determined by

$$\Gamma^{\text{out}}_{\boldsymbol{q}_j+} = \frac{2\pi}{\hbar} \frac{N^m_d}{N^2_{\text{u.c.}}} \sum_{\boldsymbol{k},\boldsymbol{k}'} \sum_{\boldsymbol{G}_m} \delta_{\boldsymbol{q}_j,\boldsymbol{k}'-\boldsymbol{k}+\boldsymbol{G}_m} |\mathcal{V}^{c\ H}_{v\ L}(\boldsymbol{k}'-\boldsymbol{k})|^2 \times (1-f_{h,\boldsymbol{k}'})(1-f_{e,\boldsymbol{k}}) \delta(\varepsilon^{\boldsymbol{k}}_e + \varepsilon^{\boldsymbol{k}'}_h - \Delta_{\boldsymbol{q}_j}), \tag{36}$$

with the typical Pauli blocking terms preventing backscattering into the substrate when the relevant states are already occupied. To obtain the total transfer rates involving all molecular exciton states, we sum over all numerically discrete $\boldsymbol{q}_j$ vectors within the first Brillouin zone of the molecules. The total rate scales linearly with the total number of molecules N_m in the system. To numerically evaluate the rate referring to one molecule (mean scattering between the inorganic semiconductor QW and one molecule of the organic layer), we calculate $\Gamma^{\text{in or out}}_{\text{tot}}/N_m$.

TABLE I. Material parameters used for calculating the transfer rates (if not varied in the plots).

L4P relative permittivity	ϵ_m	1.0
ZnO relative permittivity [62]	ϵ_s	7.9
ZnO band gap [62]	$\varepsilon^s_{\text{gap}}$	3.4 eV
2D electron density in ZnO	n^{2D}_e	$1.5\times10^{13}/\text{cm}^2$
2D hole density in ZnO	n^{2D}_h	$1.5\times10^{13}/\text{cm}^2$
Electron temperature in ZnO	T_e	10 K
Hole temperature in ZnO	T_h	10 K
Interlayer separation	Δz	0.4 nm
Molecular coverage		10×10 unit cells^2
Detuning	$\Delta_{\boldsymbol{0}}$	15 meV

For our analysis, while a parameter is varied, the other material parameters are set as given in Table I.

A. Changing the detuning

First, we examine the transfer-rate dependence on the detuning $\Delta_{\boldsymbol{q}_j=\boldsymbol{0}} \equiv \Delta_{\boldsymbol{0}} = E^{m+}_{\boldsymbol{q}_j=\boldsymbol{0}} - \varepsilon^s_{\text{gap}} - \mathcal{V}^{m\text{-}s}_{\text{mono}}$ between the renormalized resonances of the two constituents [see Fig. 6(a)]. It enters the energy-conserving δ distribution in Eqs. (35) and (36). Note that the intermolecular monopole-monopole coupling leads to a substantial energy renormalization for high molecular coverages. In the case of the closest molecular packing without steric overlap of one molecule per 6×2 substrate unit cells (see Fig. 3), we

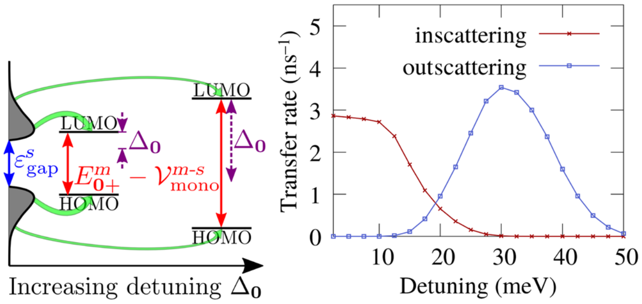

(a) (b)

FIG. 6. (a) Scheme of the system states of the semiconductor (left) and molecule (right) for increasing detuning $\Delta_{\boldsymbol{0}} = E^{m+}_{\boldsymbol{0}} - \varepsilon^s_{\text{gap}} - \mathcal{V}^{m\text{-}s}_{\text{mono}}$ (not true to scale). (b) Total in- and outscattering rates from inorganic to organic component as functions of the detuning between the renormalized resonances of the organic and inorganic constituents.

adjust the molecular gap $\varepsilon^{m}_{\mathrm{gap}}$ by several tens of meV in order to get the two exciton systems into resonance. Of course, in the case of sparse molecular coverage, the intermolecular monopole-monopole shifts have a much weaker effect. The inorganic-organic resonance energy detuning can be controlled by tuning the molecular structure (e.g., exchanging ligands, etc. [6]). Furthermore, other corrections may be important here beyond our simple model, which focuses only on the transfer. Therefore, a variation of $\Delta_{\mathbf{0}}$ [see Fig. 6(a)] is justified for obtaining a qualitative understanding of the involved transfer processes in these situations.

Figure 6(b) shows the total in- and outscattering rates as a function of the detuning $\Delta_{\mathbf{0}}$. The rates are in the range of several ns^{-1}. These values are consistent with experimentally measured transfer times of 100–300 ps in similar hybrid structures [2,6]. The inscattering rate into the molecular film decreases for an increasing $\Delta_{\mathbf{0}}$ and vanishes for detunings larger than 30 meV, so a device operation up to 10–15 meV should be efficient. By contrast, the outscattering rate has a maximum at around 30 meV and drops to zero towards higher (approximately 50 meV) and lower detunings (about 10 meV). This behavior can be understood by using the scheme of system states shown in Fig. 6(a): The carrier population in the semiconductor is depicted along the x axis as a product of the Fermi function and the density of states. The molecular states are discrete HOMO and LUMO levels with two different detunings $\Delta_{\mathbf{0}}$. (This simplified scheme ignores that the molecular system also exhibits a flat band structure due to the intermolecular Coulomb coupling. However, the molecular bands cover a very small energy range compared to the electrically pumped semiconductor states.) Low detunings mean a close energetic match between the resonances of the two constituents. This energy matching enables an efficient inscattering into the molecular layer since the semiconductor substrate exhibits a high population filling where energy and momentum conservation are fulfilled. For higher detunings and increased energy mismatch [see the right-hand side of Fig. 6(a)], the number of available scattering partners in high-energy band states decreases. Therefore, the inscattering rate shows a strong decrease. Up to $\Delta_{\mathbf{0}} = 30$ meV, the outscattering rate in Fig. 6(b) shows the opposite behavior dictated by the Pauli blocking terms that prevent backscattering. However, Pauli blocking gets weaker with increased detuning, and the outscattering rate increases until the energy mismatch between the molecular and semiconductor gap is too large to be bridged by any of the populated states in the semiconductor electron-hole continuum.

A more thorough discussion of the relevant processes in reciprocal space that determine the rate for varying detunings is given in Appendix C.

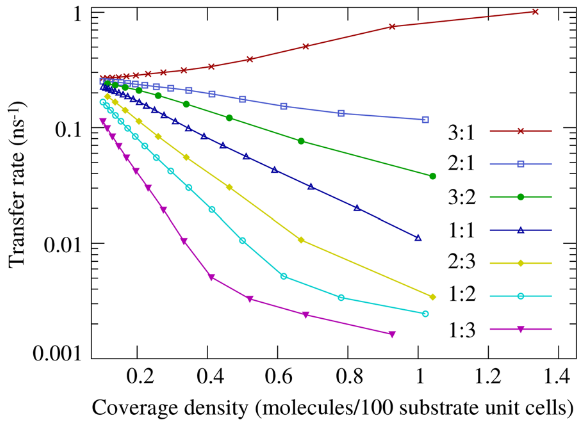

FIG. 7. Inscattering rates as functions of the molecular coverage density for different aspect ratios of the molecular coverage.

B. Influence of the molecular coverage

Figure 7 shows the excitation energy transfer rate from the electrically pumped semiconductor substrate into the molecular layer as a function of the molecular coverage density for different aspect ratios of molecular coverage. The aspect ratio $n_x{:}n_y$ defines the ratio between the number of semiconductor unit cells matching a molecular unit cell in the x direction and the number in the y direction. We calculate the transfer rate for a detuning of $\Delta_{\mathbf{0}} = 30$ meV since here a calculation over a large parameter range is feasible. Other detunings show the same overall qualitative behavior. For decreasing molecular coverages, the size of the molecular unit cell in real space increases, whereas the molecular Brillouin zone decreases [23]: The molecular reciprocal grid points get denser until a quasicontinuous density of reciprocal lattice vectors is achieved. This high reciprocal grid density increases the interlayer Coulomb coupling per molecule in the case of low molecular coverages since more processes fulfill momentum conservation. For very small coverages (the left-hand side of Fig. 7), the distance between two neighboring molecules is so large that they do not interact and the particular unit-cell geometry defined by the aspect ratio is irrelevant. Therefore, the transfer rates tend towards the same low-coverage limit independent of the aspect ratio. However, when going towards higher molecular coverage, the transfer efficiency strongly depends on the aspect ratio. Here, two processes are counteracting: On the one hand, increasing the total number of molecules per 100 substrate unit cells improves the coupling to the substrate since the coverage density given as the number of molecules divided by the number of semiconductor unit cells $N_m/N_{\mathrm{u.c.}}$ enters the rate. On the other hand, the number of allowed momentum transfer processes decreases for higher coverage due to the decreasing reciprocal grid density. The dependence on the aspect ratio reflects the spatial orientation of the molecular transition dipole moment $\boldsymbol{d}_{HL}$ along the x axis [see Fig. 4(a)]. For aspect ratios less than 1, the unit cell has a larger extent in the y direction than in the x direction, thus increasing the number of unfavorable scattering channels perpendicular to the dipole moment.

This situation leads to a weaker interaction for smaller aspect ratios. Indeed, the transfer rate decreases by orders of magnitude when increasing the molecular coverage inside typical ranges (normalized to the molecule number). This decrease is, of course, negative for the device performance. The main reason for the decrease is the smaller number of allowed transfer processes. For aspect ratios greater than 1 that coincide with the dipole orientation, this effect is strongly attenuated—and is even inverted in the case of 3 : 1 coverage. Here, the increase in transfer efficiency for high coverage dominates over the counteracting decrease of the allowed momentum transfer processes. Note that the maximum molecular coverage without steric overlap is one molecule per 6×2 substrate unit cells with an aspect ratio of 3 : 1 (see the red curve in Fig. 7). This configuration will most likely be in the experiment with one—or even multiple—fully closed organic layers on top. Here, we could show that dense coverage combined with a high aspect ratio, as in the case of maximum coverage, is advantageous for the device performance.

C. Tuning the electrical driving: Influence of the carrier concentration

In Fig. 8, the in- and outscattering transfer rates are depicted for increasing carrier concentrations in the semiconductor part. Through the chemical potential in Eq. (32), the carrier densities enter the Fermi distribution of the electron and hole continuum in the inorganic constituent. Note that here, we consider the case of electrical pumping through an injection current that equally increases the electron and hole concentrations [59], as realized, e.g., by integrating the hybrid device into a *p-i-n* configuration. However, situations with asymmetrical driving of the different carrier densities are also possible [63], which would lead to the same qualitative behavior but not be as pronounced as in the case where both charge carrier concentrations are tuned equally.

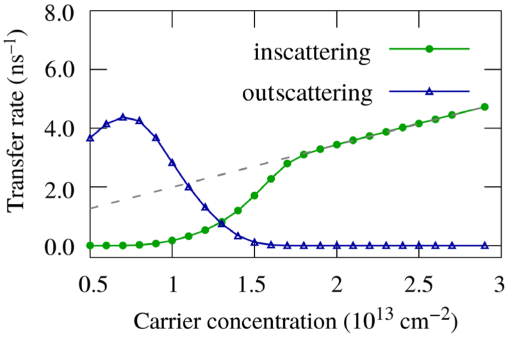

FIG. 8. Total in- and outscattering rates as functions of the two-dimensional carrier concentration in the semiconductor QW for an aspect ratio of 1 : 1 (10×10 coverage) and a charge carrier temperature of 10 K. The dashed gray line marks the linear regime that the inscattering rate enters at $n^{2D}_{e\,\mathrm{or}\,h} = 1.8 \times 10^{13}$ cm^{-2}.

The transfer efficiency is highly sensitive to the charge carrier concentration: As expected, the inscattering rate per molecule becomes larger for increasing carrier densities due to the higher number of carriers that are available as scattering partners. This effect increases the number of carriers with energies fulfilling energy conservation for transfer and thus provides an increased transfer efficiency. First, the transfer rate increases nonlinearly, then it enters a period of linear growth at $n^{2D}_{e\,\mathrm{or}\,h} = 1.8 \times 10^{13}$ cm^{-2}, indicated by the dashed gray line in Fig. 8. The initial nonlinear growth of the rate for low carrier concentrations is attributed to the energy and momentum conservation: At low $n^{2D}_{e\,\mathrm{or}\,h}$, only a few scattering channels are available in the absence of higher energy and momentum states.

With increasing carrier concentrations, the number of possible scattering partners increases until the interaction channels which are allowed by momentum and energy conservation are saturated. Then the rate enters the linear growing regime dictated simply by the constant growth of the carrier density. Surprisingly, up to $n^{2D}_{e\,\mathrm{or}\,h} = 0.7 \times 10^{13}$ cm^{-2}, the outscattering rate also increases before decreasing again. The unexpected initial growth of the outscattering rate is explained as follows: For very low carrier densities, only electronic states close to the Γ point are populated, whereas higher energy and momentum states are not occupied; see Figs. 5(c) and 5(d). This effect restricts the possible transfer processes to a small energy and momentum range, thus reducing both the in- and outscattering excitation transfer efficiency.

For increasing carrier concentrations, more electronic states contribute. However, at a certain carrier concentration, Pauli blocking is reached in the semiconductor QW and reduces the outscattering rate again: For larger carrier concentrations, an increasing number of electron-hole continuum states is occupied, thus preventing backscattering into the semiconductor layer; i.e., this process becomes negligibly small.

D. Tuning the electrical driving: Changing the carrier temperature

Figures 5(a) and 5(b) show that the temperature of the charge carriers in the QW changes the carrier distribution in the semiconductor bands considerably. To analyze the interplay between the resonance energy detuning Δ_0 and the temperatures $T_{e\,\mathrm{or}\,h}$, we calculate 2D maps for the inscattering [Fig. 9(a)] and outscattering rates [Fig. 9(c)] that depend on temperature and detuning. For higher temperatures, the in- and outgoing rates are less sensitive to resonance energy detunings, and the transfer efficiency is less dependent on the temperature.

Here, the increased population of high-energy band states in the QW at higher temperatures results in increased energy matching. This energetic match leads to a monotonic increase of the backscattering rate with increasing

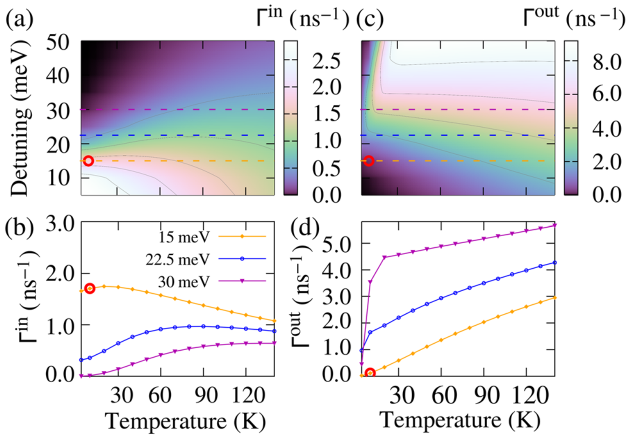

FIG. 9. Total (a) inscattering and (c) outscattering rate as a function of the charge carrier temperature $T = T_e = T_h$ and the energetic detuning Δ_0. (b),(d) Cuts through the 2D plots (a) and (c) (indicated by the dashed lines) at fixed detunings $\Delta_0 =$ 15 meV (the orange curves), 22.5 meV (the blue curves), and 30 meV (the purple curves). The red circles mark the standard values used throughout this work (see Table I).

temperature; see Figs. 9(c) and 9(d). However, an interesting feature occurs in the case of the inscattering rate; see Fig. 9(a). To highlight this effect, we additionally plot cuts through the 2D map at the fixed detunings $\Delta_0 = 15$ meV (the orange curve), 22.5 meV (the blue curve), and 30 meV (the purple curve); see Fig. 9(b). The positions of the cuts are marked by the dashed lines in the 2D map in Fig. 9(a).

For larger detunings where $\Delta_0 > 25$ meV [the upper region in the 2D map of Fig. 9(a) and the purple curve in the graph of Fig. 9(b)], the inscattering rate increases monotonically with increasing temperature, as one would expect due to the population of higher electronic states fulfilling the energy-conservation condition. By contrast, for lower detunings where $\Delta_0 < 25$ meV, the transfer rate shows a slight increase at first but then drops down again when going towards higher temperatures. Small detunings between the semiconductor band gap and molecular gap require a close energetic match that is fulfilled only by lower energy states close to the Γ point.

However, in the high-temperature regime, the population of the electron-hole continuum states close to the Γ point at $\boldsymbol{k} = 0$ decreases, whereas in turn higher energy and momentum states are occupied (see Fig. 5). This effect decreases the transfer efficiency in the case of high temperatures and small detunings. The backscattering rate in Fig. 9(b) shows the opposite behavior: The higher the detuning, the higher the backscattering efficiency. However, this behavior only holds for temperatures above 30 K. Below that, the outscattering decreases for higher detunings; see also the nonmonotonic shape of the outscattering curve in Fig. 6(b) for $T = 10$ K. Here, the large energetic detuning between the inorganic and organic parts counteracts the fact that, at low temperatures, only low-energy band states are populated.

E. Variation of the orientation and distance of the molecular film

As discussed in Sec. II C, the validity of the partial-charge technique exceeds the dipole-dipole approximation. However, effective transition dipole moments can be assigned to the partial charges belonging to one constituent according to Eqs. (14) and (15): $\boldsymbol{d}_{cv} = \sum_i q_i^{cv} \boldsymbol{r}_i$ and $\boldsymbol{d}_{LH} = \sum_j q_j^{LH} \boldsymbol{r}_j$. Therefore, we expect a dependence of the transfer efficiency on the orientation of the molecules on top of the semiconductor surface. In the geometry found by DFT calculations, the effective dipole moments of the organic and inorganic constituents both lie in the QW plane; however, they are oriented almost perpendicular. Therefore, we rotate the molecules within their plane around the vertical z axis. Figure 10(a) depicts the transfer rate in the organic film that depends on the rotational angle of the molecules around the z axis. Indeed, we observe a cos^2-like behavior with maxima at roughly 85° and 265°, where the effective dipole moments are approximately parallel. This behavior reflects the interlayer Förster coupling element entering the rate in Eq. (35) squared. Note that other parameters besides the simple cos dependence of the interlayer coupling element also play a role when rotating the molecules since the molecular band dispersion —and therefore the energy matching condition—is also altered due to the changed intermolecular coupling. Also, the rate does not drop to zero for perpendicular effective dipole moments, as one would expect for a pure dipole interaction, since there is always a substantial remaining coupling strength due to the spatial distribution of the partial charges. At perpendicular dipole moments, the rate is still around 24% of the maximum value at parallel dipoles.

Figure 10(b) shows the transfer rate into the molecular layer for an increasing distance Δz between the semiconductor substrate and the molecular adlayer. Different separations between the QW and the adsorbed organic layer can be realized experimentally, e.g., by inserting a spacer layer of variable thickness [2]. As expected, we observe a strong decrease of the transfer efficiency with increasing

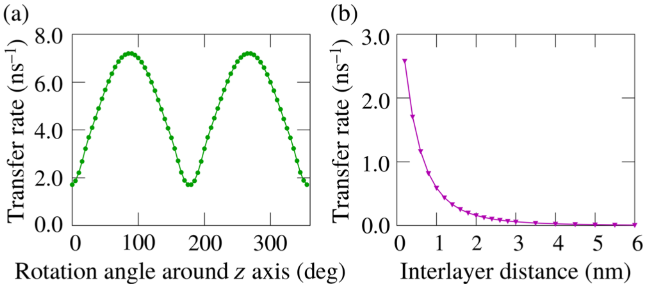

FIG. 10. (a) Total inscattering rate as a function of the rotational angle of the molecules around the z axis. (b) Total inscattering rates as functions of the interlayer separation between the semiconductor QW and the molecular layer.

interlayer separation since the interlayer Förster coupling strength entering the transfer rate is decreasing for increasing distances. Note that we do not depict the backscattering rate: It shows the same qualitative behavior.

V. CONCLUSIONS

In this paper, we use a microscopic theory for calculating the energy transfer rate from an electrically pumped inorganic semiconductor substrate into an organic molecular film. Partial charges for both the semiconductor and the molecules are obtained from DFT calculations of the electrostatic potential and are used to model the microscopic coupling elements beyond the common dipole-dipole treatment. We show that the transfer efficiency can be improved substantially by altering the geometric arrangement of the hybrid system and by varying the pumping strength. The effect of Förster coupling between the two layers is governed by the orientation of the dipole moments in the two constituents and microscopic momentum and energy selection rules, making hybrid inorganic-organic systems highly versatile building blocks for device application.

For optimizing future devices, we recommend the following guidelines: (i) Near-field effects should be exploited by using short distances, and the dipoles of the molecules and the semiconductor should be aligned. (ii) In order to suppress the backscattering, further layers of molecules with a smaller band gap should be added to act as a cascade. (iii) The carrier concentration operating point should be high enough that inscattering outweighs outscattering, and the transition energy of the molecules and the semiconductor should be aligned accordingly.

In this work, it is shown that the interlayer Coulomb coupling efficiency is governed by microscopic momentum selection rules dictated by the strict periodic arrangement of molecules on top of the ZnO substrate. However, in most experimental realizations, the molecular layer exhibits disorder that may be treated in future studies using a density-matrix approach in position space instead of a Bloch basis and introducing a molecular supercell similar to Ref. [56]. Disorder in the molecular layer is expected to relax the strict momentum selection rules, thus potentially enhancing the transfer efficiency and making the transfer rate less sensitive to changes in the molecular coverage density.

ACKNOWLEDGMENTS

We gratefully acknowledge the financial support from the Deutsche Forschungsgemeinschaft (DFG) through SFB 951 under Projects No. B4 and No. B12. This work was supported by the Academy of Finland through its Centres of Excellence Programme under Projects No. 251748 and No. 284621.

APPENDIX A: CONSTRUCTION OF PARTIAL CHARGES

The parametrization of the density-matrix formalism from the electronic structure obtained by DFT calculations was previously developed for purely crystalline semiconductor surfaces [64]. The optical excitations and the electron relaxation dynamics of silicon surfaces are calculated by a DFT parametrization based on the band structure, momentum-matrix elements, and phonon band structure obtained with a (semi)local xc functional. The first-order approximation for the Coulomb matrix elements is equivalent to the dipole matrix elements between the semiconductor and the molecular system.

The challenge is to find reliable partial charges for the molecule and the semiconductor. A simple method for cluster calculations (molecules) as well as two methods for solids (periodic boundary conditions) [25,65] is implemented in the FHI-aims code [28].

The starting point for these methods is the calculation of the electrostatic potential at a sufficiently high number of grid points outside the van der Waals (vdW) radius of the atoms [66] (defined as the radius of imaginary hard spheres reflecting the contact distance of the atoms [66]). To define a spatial region for the grid, two parameters are necessary: a minimal and a maximal radius around the atoms. These radii are defined as multiples of the vdW radius of the atoms. The values for the vdW radii of most atoms in the periodic table are taken from Refs. [67–69]. For the generation of the points, cubic (Cartesian) grids are used. For finite systems such as molecule ones, we generate points within a cube encapsulating the spheres with the maximal radius (multiple of the vdW radius) around all atoms. For periodic boundary conditions, the unit cell is used. Points within the superposition of the spheres with the minimal radius (minimal multiple of the vdW radius) are excluded.

For finite systems, we express the electrostatic potential (ESP) by a sum of Coulomb potentials with charges q_i, the partial charges, at the atomic position $\boldsymbol{r}_i$:

$$V_{\mathrm{ESP}}^{\mathrm{mol}}(\boldsymbol{r}) = \sum_{i=1}^{N_{\mathrm{at}}} \frac{q_i}{|\boldsymbol{r}-\boldsymbol{r}_i|}. \tag{A1}$$

The q_i values are calculated by a least-squares fit with the additional constraint of the constant total charge $q_{\mathrm{tot}} = \sum_{i=1}^{N_{\mathrm{at}}} q_i$. We use the method of Lagrange multipliers to minimize the function

$$F = \sum_{k=1}^{N_{\mathrm{grid}}} (V_{\mathrm{ES,DFT}}^{\mathrm{mol}}(\boldsymbol{R}_k) - V_{\mathrm{ESP}}^{\mathrm{mol}}(\boldsymbol{R}_k))^2 - \lambda\left(q_{\mathrm{tot}} - \sum_{i=1}^{N_{\mathrm{at}}} q_i\right)^2, \tag{A2}$$

where $V_{\mathrm{ES,DFT}}$ is the electrostatic potential of a DFT calculation.

For periodic systems, long-range electrostatic interactions have to be taken into account, and the potential is defined only up to an arbitrary constant [25]. The partial-charge methods implemented in this work solve these problem by Ewald summation [70]. They were developed by Campañá *et al.* [25] and further improved by Chen *et al.* [65]. The potential generated by the partial charges centered on the atoms of the unit cell then reads

$$V_{\mathrm{ESP}}^{\mathrm{solid}}(\boldsymbol{r}) = \sum_{i=1}^{N_{\mathrm{at}}} \sum_{\boldsymbol{T}} q_i \frac{\operatorname{erfc}(\alpha|\boldsymbol{r}-\boldsymbol{r}_{i,\boldsymbol{T}}|)}{|\boldsymbol{r}-\boldsymbol{r}_{i,\boldsymbol{T}}|} + \frac{4\pi}{V_{\mathrm{u.c.}}} \sum_{i=1}^{N_{\mathrm{at}}} \sum_{\boldsymbol{k}} q_i \cos[\boldsymbol{k}(\boldsymbol{r}-\boldsymbol{r}_i)] \frac{e^{-(k^2/4\alpha^2)}}{k^2}, \tag{A3}$$

where $\boldsymbol{T} = n_1\boldsymbol{a}_1 + n_2\boldsymbol{a}_2 + n_3\boldsymbol{a}_3$ represents the real-space translation vectors of the lattice vectors $\boldsymbol{a}_i$ and $n_i \in \mathbb{Z}$. $\boldsymbol{k} = m_1\boldsymbol{b}_1 + m_2\boldsymbol{b}_2 + m_3\boldsymbol{b}_3$ is the reciprocal-space translation vector and $\boldsymbol{b_i}$ indicates the reciprocal lattice vectors with $m_i \in \mathbb{Z}$. $V_{\mathrm{u.c.}}$ is the volume of the unit cell. The parameter α is defined as $\alpha = (\sqrt{\pi}/R_c)$, with R_c being the cutoff radius of the Ewald summation [70]. The function to minimize is [65]

$$F^{\mathrm{PBC}} = \sum_{k=1}^{N_{\mathrm{grid}}} [V_{\mathrm{DFT}}^{\mathrm{solid}}(\boldsymbol{R}_k) - (V_{\mathrm{ESP}}^{\mathrm{solid}}(\boldsymbol{R}_k) + V_{\mathrm{offset}})]^2 - \lambda\left(q_{\mathrm{tot}} - \sum_{i=1}^{N_{\mathrm{at}}} q_i\right) + \beta \sum_{i=1}^{N_{\mathrm{at}}} (q_i - q_{i0})^2. \tag{A4}$$

Here, the arbitrary offset of the potential V_{offset} is an additional fitting parameter. The constraint charges q_{i0} can be determined with other methods (e.g., Mulliken charge analysis [71]). β is a weighting factor.

APPENDIX B: CALCULATION OF THE EIGENPROBLEM OF THE MOLECULAR EXCITONS

The eigenproblem for the molecular excitons reads

$$\langle \boldsymbol{l}+\boldsymbol{q},\boldsymbol{l}|(\hat{H}_0^m + \hat{H}_C^{m\text{-}m})|X_\alpha^m\rangle = (E_0^m + E_\alpha^m)c_{\boldsymbol{l}+\boldsymbol{q},\boldsymbol{l}}^\alpha. \tag{B1}$$

For a sufficiently large material sample, the molecular wave vectors are continuous, and the sums can be transformed into two-dimensional integrals according to

$$\sum_{\boldsymbol{l}} \to \frac{N_m A_m}{(2\pi)^2} \int d^2 l, \tag{B2}$$

where A_m denotes the area of one molecular unit cell. Exploiting the lattice periodicity of the Coulomb coupling elements in momentum space, we find

$$\begin{aligned} E_\alpha^m c_{\boldsymbol{l}+\boldsymbol{q},\boldsymbol{l}}^\alpha = c_{\boldsymbol{l}+\boldsymbol{q},\boldsymbol{l}}^\alpha \Big\{ & \varepsilon_{\mathrm{gap}}^m - \mathcal{V}_{H\,H}^{H\,H}(\boldsymbol{0}) + \mathcal{V}_{H\,L}^{H\,L}(\boldsymbol{0}) \\ & + \frac{A_m}{4\pi^2} \int d^2 l' [\mathcal{V}_{H\,H}^{H\,H}(\boldsymbol{l}') - \mathcal{V}_{L\,H}^{H\,L}(\boldsymbol{l}')] \Big\} \\ & + \frac{A_m}{4\pi^2} \int d^2 l' c_{\boldsymbol{l}'+\boldsymbol{q},\boldsymbol{l}'}^\alpha [\mathcal{V}_{L\,H}^{H\,L}(\boldsymbol{q}) - \mathcal{V}_{H\,L}^{H\,L}(\boldsymbol{l}'-\boldsymbol{l})], \end{aligned} \tag{B3}$$

with $\varepsilon_{\mathrm{gap}}^m = \varepsilon_L - \varepsilon_H$. To make the problem numerically tractable, the continuous wave vectors are discretized. Therefore, the integrals over the first BZ are rewritten into sums over N_d^m small surface segments of size $\Delta A \equiv \frac{A_{\mathrm{BZ}}^m}{N_d^m}$:

$$\int d^2 l' f(\boldsymbol{l}') \to \sum_{i=1}^{N_d^m} \Delta A f(\boldsymbol{l}_i). \tag{B4}$$

Moreover, we approximate $\mathcal{V}_{H\,L}^{H\,L}(\boldsymbol{l}'-\boldsymbol{l}) \approx \mathcal{V}_{H\,L}^{H\,L}(\boldsymbol{0})$ in the last line of Eq. (B3) since the variation of the monopole-monopole coupling elements $\mathcal{V}_{H\,L}^{H\,L}$ within the first BZ is small (only a few percent). This approximation reduces the complexity of the eigenproblem and we can derive the eigenproblem for the energy E_α^m and the coefficients $c_{\boldsymbol{l}_i+\boldsymbol{q}_j,\boldsymbol{l}_i}^{\boldsymbol{q}}$ in matrix form. It is diagonal with respect to the momentum transfer $\boldsymbol{q}_j$, yielding a block-diagonal form for the entire index space $(\boldsymbol{l}_i, \boldsymbol{q}_j)$. We use the abbreviations

$$a_{\boldsymbol{q}_j} = \frac{1}{N_d^m} [\mathcal{V}_{L\,H}^{H\,L}(\boldsymbol{q}_j) - \mathcal{V}_{H\,L}^{H\,L}(\boldsymbol{0})], \tag{B5}$$

$$d_{\boldsymbol{q}_j} \equiv a_{\boldsymbol{q}_j} + \varepsilon_{\mathrm{gap}}^m - \mathcal{V}_{H\,H}^{H\,H}(\boldsymbol{0}) + \mathcal{V}_{H\,L}^{H\,L}(\boldsymbol{0}) + \frac{1}{N_d^m} \sum_{k=1}^{N_d^m} [\mathcal{V}_{H\,H}^{H\,H}(\boldsymbol{l}_k) - \mathcal{V}_{L\,H}^{H\,L}(\boldsymbol{l}_k)]. \tag{B6}$$

Each $N_d^m \times N_d^m$ block for a given $\boldsymbol{q}_j$ has the form

$$E_{\boldsymbol{q}_j}^m \begin{pmatrix} c_{\boldsymbol{l}_1}^{\boldsymbol{q}_j} \\ c_{\boldsymbol{l}_2}^{\boldsymbol{q}_j} \\ \vdots \\ c_{\boldsymbol{l}_{N_d^m}}^{\boldsymbol{q}_j} \end{pmatrix} = \begin{pmatrix} d_{\boldsymbol{q}_j} & a_{\boldsymbol{q}_j} & \cdots & a_{\boldsymbol{q}_j} \\ a_{\boldsymbol{q}_j} & \ddots & & \vdots \\ \vdots & & \ddots & a_{\boldsymbol{q}_j} \\ a_{\boldsymbol{q}_j} & \cdots & a_{\boldsymbol{q}_j} & d_{\boldsymbol{q}_j} \end{pmatrix} \begin{pmatrix} c_{\boldsymbol{l}_1}^{\boldsymbol{q}_j} \\ c_{\boldsymbol{l}_2}^{\boldsymbol{q}_j} \\ \vdots \\ c_{\boldsymbol{l}_{N_d^m}}^{\boldsymbol{q}_j} \end{pmatrix}, \tag{B7}$$

with the eigenvector components abbreviated by $c_{\boldsymbol{l}_i}^{\boldsymbol{q}_j} \equiv c_{\boldsymbol{l}_i+\boldsymbol{q}_j,\boldsymbol{l}_i}^{\boldsymbol{q}_j}$. Note that they are defined only for wave-vector sums $\boldsymbol{l}_i + \boldsymbol{q}_j$ within the first BZ. If $\boldsymbol{l}_i + \boldsymbol{q}_j$ exceeds the first BZ, it is mapped back into the first BZ by means of a reciprocal lattice vector.

This highly symmetric eigenproblem in matrix form can be solved analytically. It has two eigenvalues:

$$E_-^m = E^m_{\boldsymbol{q}_j,n=1} = \cdots = E^m_{\boldsymbol{q}_j,n=N_d^m-1} = d_{\boldsymbol{q}_j} - a_{\boldsymbol{q}_j}, \tag{B8}$$

$$E^m_{\boldsymbol{q}_j+} = E^m_{\boldsymbol{q}_j,n=N_d^m} = d_{\boldsymbol{q}_j} + (N_d^m - 1)a_{\boldsymbol{q}_j}. \tag{B9}$$

E_-^m is $(N_d^m - 1)$-fold degenerate.

The $(N_d^m - 1)$ eigenvectors belonging to $E^{m-}_{\boldsymbol{q}_j}$ are enumerated by $n \in \{1, \ldots, N_d^m - 1\}$. Their normalized components are given by

$$c_{\boldsymbol{l}_i}^{\boldsymbol{q}_j,n} = \frac{N_d^m}{N_m} \times \begin{cases} \frac{1}{\sqrt{2}} & \text{for } i = 1, \\ -\frac{1}{\sqrt{2}} & \text{for } i = n+1, \\ 0 & \text{otherwise.} \end{cases} \tag{B10}$$

The nondegenerate eigenvalue $E^m_{\boldsymbol{q}_j+}$ has identical normalized eigenvector components $c_{\boldsymbol{l}_i}^{\boldsymbol{q}_j,n=N_d^m} = (\sqrt{N_d^m}/N_m)$ for all values of i.

APPENDIX C: RECIPROCAL-SPACE ANALYSIS OF THE RATES FOR VARIOUS DETUNINGS

To understand the behavior of the in- and outscattering transfer rate for various detunings, we analyze the individual transfer rates $\Gamma^{\text{in or out}}_{\boldsymbol{q}_j+}$ that depend on the molecular transfer vector $\boldsymbol{q}_j$. The individual transfer rates are summed up for the total rates in Fig. 6(b). To enhance our understanding, we define the in- and outscattering Fermi factors $f^{\text{in}}_{\boldsymbol{q}_j+}$ and $f^{\text{out}}_{\boldsymbol{q}_j+}$, respectively, as the sums over the products of Fermi functions, which obey the δ conditions for momentum and energy conservation of the transfer rates:

$$f^{\text{in}}_{\boldsymbol{q}_j+} = \sum_{\boldsymbol{k},\boldsymbol{k}'} \sum_{\boldsymbol{G}_m} f_{h,\boldsymbol{k}'} f_{e,\boldsymbol{k}} \delta_{\boldsymbol{q}_j,\boldsymbol{k}'-\boldsymbol{k}+\boldsymbol{G}_m} \delta(\varepsilon_e^{\boldsymbol{k}} + \varepsilon_h^{\boldsymbol{k}'} - \Delta_{\boldsymbol{q}_j}), \tag{C1}$$

$$f^{\text{out}}_{\boldsymbol{q}_j+} = \sum_{\boldsymbol{k},\boldsymbol{k}'} \sum_{\boldsymbol{G}_m} (1 - f_{h,\boldsymbol{k}'})(1 - f_{e,\boldsymbol{k}}) \delta_{\boldsymbol{q}_j,\boldsymbol{k}'-\boldsymbol{k}+\boldsymbol{G}_m} \times \delta(\varepsilon_e^{\boldsymbol{k}} + \varepsilon_h^{\boldsymbol{k}'} - \Delta_{\boldsymbol{q}_j}). \tag{C2}$$

These Fermi factors give a good estimate of the population filling from the $\boldsymbol{q}$-space regions defined by momentum and energy conservation. Figures 11 and 12 show the $\boldsymbol{q}$-dependent in- and outscattering rates (left columns), respectively, and the corresponding Fermi factors (right columns) for increasing detunings $\boldsymbol{\Delta_0}$ of 10 meV [Figs. 11(a) and 12(a)], 20 meV [Figs. 11(b) and 12(b)], and 30 meV [Figs. 11(c) and 12(c)]. In the case of low detuning, $\boldsymbol{\Delta_0} = 10$ meV, the inscattering Fermi factor [see Fig. 11(a), right panel] shows a consistently high contribution over the full range of possible momentum transfer $\boldsymbol{q}$ vectors within the first-molecule Brillouin zone. This high value is due to the close energetic match between the resonances of the two constituents, as illustrated for the system states in Fig. 6(a): For matching resonance energies (the left-hand HOMO-LUMO system), an efficient inscattering into the molecular film is possible because the bands of the ZnO substrate are highly filled in the regions that obey energy and momentum conservation for the transfer process to the molecular system.

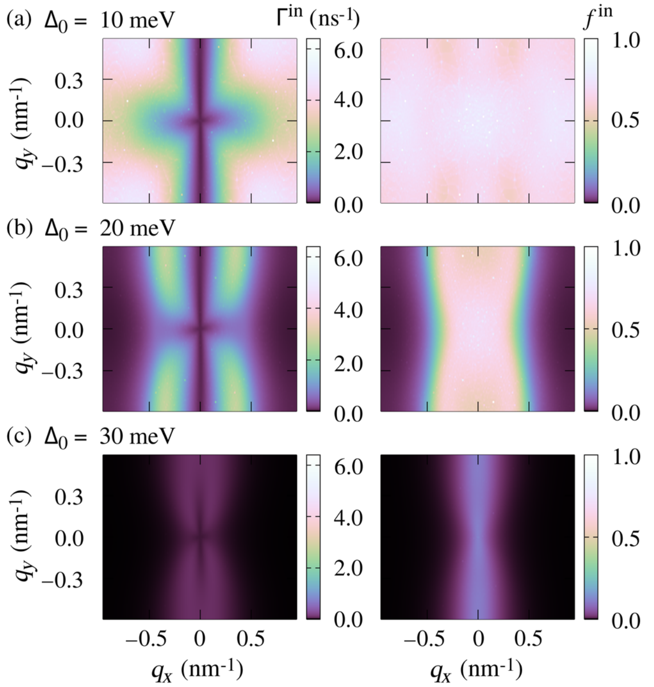

FIG. 11. Inscattering rates $\Gamma^{\text{in}}_{\boldsymbol{q}_j+}$ (left column) and Fermi factors $f^{\text{in}}_{\boldsymbol{q}_j+}$ (right column) for increasing resonance energy detuning $\boldsymbol{\Delta_0}$ of (a) 10, (b) 20, and (c) 30 meV. The displayed $\boldsymbol{q}$ range reflects the size of the first-molecule Brillouin zone for a coverage of one molecule per 10 × 10 substrate unit cells. The molecular system, despite exhibiting a band structure, is simplified to a two-level system since we focus on the energy at $\boldsymbol{q} = 0$.

However, the contributing regions determined by the inscattering Fermi factor (see the right column of Fig. 11) shrink considerably for an increased detuning since the number of scattering partners fulfilling the energy conservation decreases substantially; see the HOMO-LUMO systems in Fig. 6(a). The decrease of scattering partners occurs mainly along the x direction. The reason for the decrease along the x direction is found in the $\boldsymbol{q}$-dependent intermolecular Förster coupling element $\mathcal{V}^{H\,L}_{L\,H}(\boldsymbol{q}_j)$ shown in Fig. 4(a): Caused by the molecular dipole, the coupling element shows dumbbell-shaped maxima along the x axis at the borders of the molecular Brillouin zone, i.e., around $q_y = 0$ and $q_x = \pm\tilde{b}_1/2$. (Here, $\tilde{\boldsymbol{b}}_1$ is the molecular reciprocal lattice vector pointing in the x direction.)

Correspondingly, the molecular eigenenergy $E^m_{\boldsymbol{q}_j+} \propto \mathcal{V}^{H\,L}_{L\,H}(\boldsymbol{q}_j)$ in the energy conservation shows maxima in these areas of momentum transfer. This effect further increases the energy difference $\Delta_{\boldsymbol{q}_j} = E^m_{\boldsymbol{q}_j+} - \varepsilon^s_{\text{gap}} - \mathcal{V}^{m\text{-}s}_{\text{mono}}$ and leads to a reduced energy match. Thus, the inscattering efficiency decreases for large detunings and reflects the

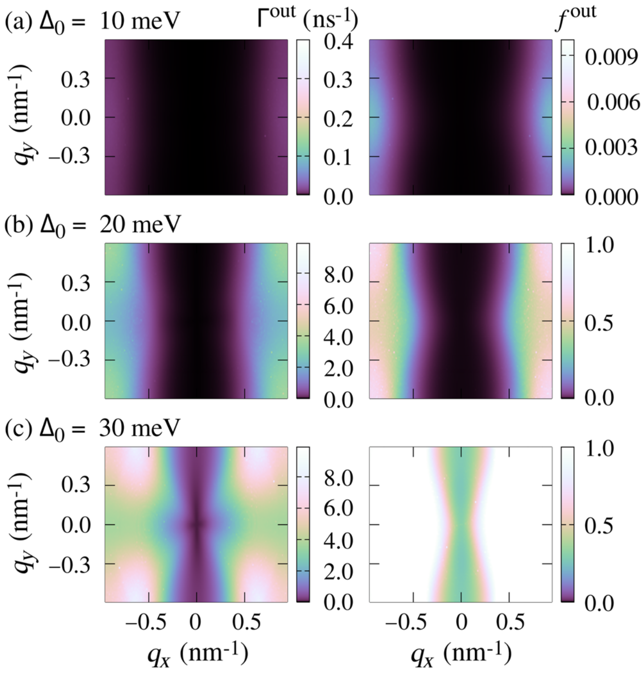

FIG. 12. Outscattering rates $\Gamma^{\text{out}}_{\boldsymbol{q}_j+}$ (left column) and Fermi factors $f^{\text{out}}_{\boldsymbol{q}_j+}$ (right column) for increasing resonance energy detuning Δ_0 of (a) 10, (b) 20, and (c) 30 meV. The displayed $\boldsymbol{q}$ range reflects the size of the first-molecule Brillouin zone for a coverage of one molecule per 10×10 substrate unit cells.

reduced occupation in the relevant energetic region (see the right column of Fig. 11).

The inscattering rates (see the left column of Fig. 11) are reduced in the central region around $\boldsymbol{q} = 0$ for all detunings, which is not explained by the Fermi factors alone. This reduction is caused by the interlayer Förster coupling element entering the transfer rate in Eq. (35). The matrix element shows four lobes along the diagonals, with vanishing coupling in the center [see Fig. 4(b)]. This form is reflected in the transfer rate. Note that discrete contributions are visible as sharp spots in the rather continuous inscattering Fermi factors in Fig. 11. These discrete points might appear as a consequence of the discrete molecular positions in the periodic hybrid structure considered here, similar to the patterned observables in x-ray diffraction experiments probing the elastic scattering at crystalline structures.

As expected, the opposite behavior is observed for the outscattering rate and outscattering Fermi factors; see Fig. 12. In the outscattering Fermi factor (the right column of Fig. 12), the area where Pauli blocking prevents scattering is decreased for increased detunings, which increases the outscattering rate (the left column of Fig. 12). The outscattering rate decreases again for detunings larger than 30 meV. Here, the energy mismatch between the molecular gap and the semiconductor band gap is larger than the energy difference between any of the populated states in the semiconductor electron-hole continuum.

[1] D. Basko, G. C. La Rocca, F. Bassani, and V. M. Agranovich, Förster energy transfer from a semiconductor quantum well to an organic material overlayer, Eur. Phys. J. B **8**, 353 (1999).

[2] S. Blumstengel, S. Sadofev, C. Xu, J. Puls, and F. Henneberger, Converting Wannier into Frenkel Excitons in an Inorganic/Organic Hybrid Semiconductor Nanostructure, Phys. Rev. Lett. **97**, 237401 (2006).

[3] G. Itskos, G. Heliotis, P. G. Lagoudakis, J. Lupton, N. P. Barradas, E. Alves, S. Pereira, I. M. Watson, M. D. Dawson, J. Feldmann, R. Murray, and D. D. C. Bradley, Efficient dipole-dipole coupling of Mott-Wannier and Frenkel excitons in (Ga,In)N quantum well/polyfluorene semiconductor heterostructures, Phys. Rev. B **76**, 035344 (2007).

[4] A. A. R. Neves, A. Camposeo, R. Cingolani, and D. Pisignano, Interaction scheme and temperature behavior of energy transfer in a light-emitting inorganic-organic composite system, Adv. Funct. Mater. **18**, 751 (2008).

[5] T. Liang, Y. Cui, J. Yu, W. Lin, Y. Yang, and G. Qian, Large nonlinear optical activity from hybrid inorganic-organic films with fluorinated benzene as isolation group, Thin Solid Films **544**, 407 (2013).

[6] R. Schlesinger, F. Bianchi, S. Blumstengel, C. Christodoulou, R. Ovsyannikov, B. Kobin, K. Moudgil, S. Barlow, S. Hecht, S. R. Marder *et al.*, Efficient light emission from inorganic and organic semiconductor hybrid structures by energy-level tuning, Nat. Commun. **6**, 6754 (2015).

[7] Y. Qiao, F. Polzer, H. Kirmse, E. Steeg, S. Kühn, S. Friede, S. Kirstein, and J. P. Rabe, Nanotubular *J*-aggregates and quantum dots coupled for efficient resonance excitation energy transfer, ACS Nano **9**, 1552 (2015).

[8] S. Friede, S. Kuehn, S. Sadofev, S. Blumstengel, F. Henneberger, and T. Elsaesser, Nanoscale transport of surface excitons at the interface between ZnO and a molecular monolayer, Phys. Rev. B **91**, 121415 (2015).

[9] M. P. Ljungberg, O. Vänskä, P. Koval, S. W. Koch, M. Kira, and D. Sánchez-Portal, Charge-transfer states and optical transitions at the pentacene-TiO$_2$ interface, New J. Phys. **19**, 033019 (2017).

[10] H. Haug and S. W. Koch, *Quantum Theory of the Optical and Electronic Properties of Semiconductors* (World Scientific, Singapore, 2004).

[11] S. Nakamura, M. Senoh, N. Iwasa, and S.-i. Nagahama, High-brightness InGaN blue, green and yellow light-emitting diodes with quantum well structures, Jpn. J. Appl. Phys. **34**, L797 (1995).

[12] R. Zimmermann, F. Grosse, and E. Runge, Excitons in semiconductor nanostructures with disorder, Pure Appl. Chem. **69**, 1179 (1997).

[13] R. Zimmermann, E. Runge, and V. Savona, in *Quantum Coherence Correlation and Decoherence in Semiconductor Nanostructures*, edited by T. Takagahara (Elsevier Science, New York, 2003), p. 89.

[14] R. Singh, M. Richter, G. Moody, M. E. Siemens, H. Li, and S. T. Cundiff, Localization dynamics of excitons in disordered semiconductor quantum wells, Phys. Rev. B **95**, 235307 (2017).

[15] V. M. Agranovich, D. M. Basko, G. C. La Rocca, and F. Bassani, Excitons and optical nonlinearities in hybrid

organic-inorganic nanostructures, J. Phys. Condens. Matter **10**, 9369 (1998).

[16] M. Richter, Nanoplatelets as material system between strong confinement and weak confinement, Phys. Rev. Mater. **1**, 016001 (2017).

[17] Y. Vaynzof, A. A. Bakulin, S. Gélinas, and R. H. Friend, Direct Observation of Photoinduced Bound Charge-Pair States at an Organic-Inorganic Semiconductor Interface, Phys. Rev. Lett. **108**, 246605 (2012).

[18] F. Piersimoni, R. Schlesinger, J. Benduhn, D. Spoltore, S. Reiter, I. Lange, N. Koch, K. Vandewal, and D. Neher, Charge transfer absorption and emission at ZnO/organic interfaces, J. Phys. Chem. Lett. **6**, 500 (2015).

[19] Th. Förster, Intermolecular energy migration and fluorescence, Ann. Phys. (Berlin) **437**, 55 (1948).

[20] S. Blumstengel, S. Sadofev, and F. Henneberger, Electronic coupling of optical excitations in organic/inorganic semiconductor hybrid structures, New J. Phys. **10**, 065010 (2008).

[21] T. Plehn, D. Ziemann, J. Megow, and V. May, Frenkel to Wannier-Mott exciton transition: Calculation of FRET rates for a tubular dye aggregate coupled to a CdSe nanocrystal, J. Phys. Chem. B **119**, 7467 (2015).

[22] V. Agranovich, R. Atanasov, and F. Bassani, Hybrid interface excitons in organic-inorganic quantum wells, Solid State Commun. **92**, 295 (1994).

[23] E. Verdenhalven, A. Knorr, M. Richter, B. Bieniek, and P. Rinke, Theory of optical excitations in dipole-coupled hybrid molecule-semiconductor layers: Coupling of a molecular resonance to semiconductor continuum states, Phys. Rev. B **89**, 235314 (2014).

[24] M. E. Madjet, A. Abdurahman, and T. Renger, Intermolecular Coulomb couplings from *ab initio* electrostatic potentials: Application to optical transitions of strongly coupled pigments in photosynthetic antennae and reaction centers, J. Phys. Chem. B **110**, 17268 (2006).

[25] C. Campañá, B. Mussard, and T. K. Woo, Electrostatic potential derived atomic charges for periodic systems using a modified error functional, J. Chem. Theory Comput. **5**, 2866 (2009).

[26] B. Kobin, L. Grubert, S. Blumstengel, F. Henneberger, and S. Hecht, Vacuum-processable ladder-type oligophenylenes for organic-inorganic hybrid structures: Synthesis, optical and electrochemical properties upon increasing planarization as well as thin film growth, J. Mater. Chem. **22**, 4383 (2012).

[27] J. Heyd, G. E. Scuseria, and M. Ernzerhof, Hybrid functionals based on a screened Coulomb potential, J. Chem. Phys. **118**, 8207 (2003).

[28] V. Blum, R. Gehrke, F. Hanke, P. Havu, V. Havu, X. Ren, K. Reuter, and M. Scheffler, *Ab initio* molecular simulations with numeric atom-centered orbitals, Comput. Phys. Commun. **180**, 2175 (2009).

[29] X. Ren, P. Rinke, V. Blum, J. Wieferink, A. Tkatchenko, A. Sanfilippo, K. Reuter, and M. Scheffler, Resolution-of-identity approach to Hartree-Fock, hybrid density functionals, RPA, MP2 and *GW* with numeric atom-centered orbital basis functions, New J. Phys. **14**, 053020 (2012).

[30] S. V. Levchenko, X. Ren, J. Wieferink, R. Johanni, P. Rinke, V. Blum, and M. Scheffler, Hybrid functionals for large periodic systems in an all-electron, numeric atom-centered basis framework, Comput. Phys. Commun. **192**, 60 (2015).

[31] L. Bengtsson, Dipole correction for surface supercell calculations, Phys. Rev. B **59**, 12301 (1999).

[32] A. Tkatchenko and M. Scheffler, Accurate Molecular Van Der Waals Interactions from Ground-State Electron Density and Free-Atom Reference Data, Phys. Rev. Lett. **102**, 073005 (2009).

[33] G.-X. Zhang, A. Tkatchenko, J. Paier, H. Appel, and M. Scheffler, Van Der Waals Interactions in Ionic and Semiconductor Solids, Phys. Rev. Lett. **107**, 245501 (2011).

[34] O. T. Hofmann, J.-C. Deinert, Y. Xu, P. Rinke, J. Stähler, M. Wolf, and M. Scheffler, Large work function reduction by adsorption of a molecule with a negative electron affinity: Pyridine on ZnO$(10\bar{1}0)$, J. Chem. Phys. **139**, 174701 (2013).

[35] B. Bieniek, O. T. Hofmann, and P. Rinke, Influence of hydrogen on the structure and stability of ultra-thin ZnO on metal substrates, Appl. Phys. Lett. **106**, 131602 (2015).

[36] M. Richter, K. J. Ahn, A. Knorr, A. Schliwa, D. Bimberg, M. E. Madjet, and T. Renger, Theory of excitation transfer in coupled nanostructures—From quantum dots to light harvesting complexes, Phys. Status Solidi B **243**, 2302 (2006).

[37] J. D. Jackson, *Classical Electrodynamics*, 3rd ed. (John Wiley & Sons, New York, 1999).

[38] J. Specht, E. Verdenhalven, S. Theuerholz, A. Knorr, and M. Richter, Theory of coupled hybrid inorganic/organic systems: Excitation transfer at semiconductor/molecule interfaces, Proc. SPIE Int. Soc. Opt. Eng. **9746**, 97460F (2016).

[39] B. W. Lovett, J. H. Reina, A. Nazir, and G. A. D. Briggs, Optical schemes for quantum computation in quantum dot molecules, Phys. Rev. B **68**, 205319 (2003).

[40] J. Danckwerts, K. J. Ahn, J. Förstner, and A. Knorr, Theory of ultrafast nonlinear optics of Coulomb-coupled semiconductor quantum dots: Rabi oscillations and pump-probe spectra, Phys. Rev. B **73**, 165318 (2006).

[41] C. Curutchet, A. Franceschetti, A. Zunger, and G. D. Scholes, Examining Förster energy transfer for semiconductor nanocrystalline quantum dot donors and acceptors, J. Phys. Chem. C **112**, 13336 (2008).

[42] P. Machnikowski and E. Rozbicki, Phonon-assisted excitation transfer in quantum dot molecules: From quantum kinetics to transfer rates, Phys. Status Solidi B **246**, 320 (2009).

[43] J. F. Specht, A. Knorr, and M. Richter, Two-dimensional spectroscopy: An approach to distinguish Förster and Dexter transfer processes in coupled nanostructures, Phys. Rev. B **91**, 155313 (2015).

[44] F. A. Momany, Determination of partial atomic charges from *ab initio* molecular electrostatic potentials. application to formamide, methanol, and formic acid, J. Phys. Chem. **82**, 592 (1978).

[45] S. R. Cox and D. E. Williams, Representation of the molecular electrostatic potential by a net atomic charge model, J. Comput. Chem. **2**, 304 (1981).

[46] U. C. Singh and P. A. Kollman, An approach to computing electrostatic charges for molecules, J. Comput. Chem. **5**, 129 (1984).

[47] B. H. Besler, K. M. Merz, and P. A. Kollman, Atomic charges derived from semiempirical methods, J. Comput. Chem. **11**, 431 (1990).

[48] L. E. Chirlian and M. M. Francl, Atomic charges derived from electrostatic potentials: A detailed study, J. Comput. Chem. **8**, 894 (1987).

[49] C. M. Breneman and K. B. Wiberg, Determining atom-centered monopoles from molecular electrostatic potentials. The need for high sampling density in formamide conformational analysis, J. Comput. Chem. **11**, 361 (1990).

[50] C. I. Bayly, P. Cieplak, W. Cornell, and P. A. Kollman, A well-behaved electrostatic potential based method using charge restraints for deriving atomic charges: The RESP model, J. Phys. Chem. **97**, 10269 (1993).

[51] E. Sigfridsson and U. Ryde, Comparison of methods for deriving atomic charges from the electrostatic potential and moments, J. Comput. Chem. **19**, 377 (1998).

[52] H. Hu, Z. Lu, and W. Yang, Fitting molecular electrostatic potentials from quantum mechanical calculations, J. Chem. Theory Comput. **3**, 1004 (2007).

[53] G. D. Scholes, Long-range resonance energy transfer in molecular systems, Annu. Rev. Phys. Chem. **54**, 57 (2003).

[54] B. Delley, An all-electron numerical method for solving the local density functional for polyatomic molecules, J. Chem. Phys. **92**, 508 (1990).

[55] B. Delley, High order integration schemes on the unit sphere, J. Comput. Chem. **17**, 1152 (1996).

[56] E. Malic, C. Weber, M. Richter, V. Atalla, T. Klamroth, P. Saalfrank, S. Reich, and A. Knorr, Microscopic Model of the Optical Absorption of Carbon Nanotubes Functionalized with Molecular Spiropyran Photoswitches, Phys. Rev. Lett. **106**, 097401 (2011).

[57] J. C. Slater, The electronic structure of metals, Rev. Mod. Phys. **6**, 209 (1934).

[58] W. W. Chow, S. W. Koch, and M. Sargent III, *Semiconductor-Laser Physics* (Springer Science+Business Media, New York, 2012).

[59] W. W. Chow and S. W. Koch, *Semiconductor-Laser Fundamentals: Physics of the Gain Materials* (Springer, Berlin, 1999).

[60] J. Wolters, M.-R. Dachner, E. Malić, M. Richter, U. Woggon, and A. Knorr, Carrier heating in light-emitting quantum-dot heterostructures at low injection currents, Phys. Rev. B **80**, 245401 (2009).

[61] E. Malic, M. Richter, G. Hartmann, J. Gomis-Bresco, U. Woggon, and A. Knorr, Analytical description of gain depletion and recovery in quantum dot optical amplifiers, New J. Phys. **12**, 063012 (2010).

[62] H. Yoshikawa and S. Adachi, Optical constants of ZnO, Jpn. J. Appl. Phys. **36**, 6237 (1997).

[63] K. Lüdge, M. J. P. Bormann, E. Malić, P. Hövel, M. Kuntz, D. Bimberg, A. Knorr, and E. Schöll, Turn-on dynamics and modulation response in semiconductor quantum dot lasers, Phys. Rev. B **78**, 035316 (2008).

[64] N. Buecking, P. Kratzer, M. Scheffler, and A. Knorr, Linking density functional and density-matrix theory: Picosecond electron relaxation at the Si(100) surface, Phys. Rev. B **77**, 233305 (2008).

[65] D.-L. Chen, A. C. Stern, B. Space, and J. K. Johnson, Atomic charges derived from electrostatic potentials for molecular and periodic systems, J. Phys. Chem. A **114**, 10225 (2010).

[66] L. Pauling, *The Nature of the Chemical Bond and the Structure of Molecules and Crystals: An Introduction to Modern Structural Chemistry*, 3rd ed. (Cornell University Press, Ithaca, 1960).

[67] A. Bondi, Van der Waals volumes and radii, J. Phys. Chem. **68**, 441 (1964).

[68] R. S. Rowland and R. Taylor, Intermolecular nonbonded contact distances in organic crystal structures: Comparison with distances expected from van der Waals radii, J. Phys. Chem. **100**, 7384 (1996).

[69] M. Mantina, A. C. Chamberlin, R. Valero, C. J. Cramer, and D. G. Truhlar, Consistent van der Waals radii for the whole main group, J. Phys. Chem. A **113**, 5806 (2009).

[70] P. P. Ewald, Calculation of optical and electrostatic grid potentials, Ann. Phys. (Berlin) **369**, 253 (1921).

[71] R. S. Mulliken, Electronic population analysis on LCAO-MO molecular wave functions. I, J. Chem. Phys. **23**, 1833 (1955).